Ann. Geophys., 34, 1209–1229, 2016
www.ann-geophys.net/34/1209/2016/
doi:10.5194/angeo-34-1209-2016

Annales Geophysicae Open Access EGU

Derivation of turbulent energy dissipation rate with the Middle Atmosphere Alomar Radar System (MAARSY) and radiosondes at Andøya, Norway

Qiang Li[1], Markus Rapp[1,a], Anne Schrön[2], Andreas Schneider[2], and Gunter Stober[2]

[1]Deutsches Zentrum für Luft- und Raumfahrt, Institut für Physik der Atmosphäre, 82234 Oberpfaffenhofen, Germany
[2]Leibniz-Institut für Atmosphärenphysik, 18225 Kühlungsborn, Germany
[a]also at: Meteorologisches Institut München, Ludwig-Maximilians-Universität München, Munich, Germany

Correspondence to: Qiang Li (qiang.li@dlr.de)

Received: 4 May 2016 – Revised: 8 November 2016 – Accepted: 23 November 2016 – Published: 16 December 2016

Abstract. We present the derivation of turbulent energy dissipation rate ε from a total of 522 days of observations with the Middle Atmosphere Alomar Radar SYstem (MAARSY) mesosphere–stratosphere–troposphere (MST) radar running tropospheric experiments during the period of 2010–2013 as well as with balloon-borne radiosondes based on a campaign in the summer 2013. Spectral widths are converted to ε after the removal of the broadening effects due to the finite beam width of the radar. With the simultaneous in situ measurements of ε with balloon-borne radiosondes at the MAARSY radar site, we compare the ε values derived from both techniques and reach an encouraging agreement between them. Using all the radar data available, we present a preliminary climatology of atmospheric turbulence in the UTLS (upper troposphere and lower stratosphere) region above the MAARSY site showing a variability of more than 5 orders of magnitude inherent in turbulent energy dissipation rates. The derived ε values reveal a log-normal distribution with a negative skewness, and the ε profiles show an increase with height which is also the case for each individual month. Atmospheric turbulence based on our radar measurements reveals a seasonal variation but no clear diurnal variation in the UTLS region. Comparison of ε with the gradient Richardson number Ri shows that only 1.7 % of all the data with turbulence occur under the condition of $Ri < 1$ and that the values of ε under the condition of $Ri < 1$ are significantly larger than those under $Ri > 1$. Further, there is a roughly negative correlation between ε and Ri that is independent of the scale dependence of Ri. Turbulence under active dynamical conditions (velocity of horizontal wind $U > 10\,\mathrm{m\,s^{-1}}$) is significantly stronger than under quiet conditions ($U < 10\,\mathrm{m\,s^{-1}}$). Last but not least, the derived ε values are compared with the corresponding vertical shears of background wind velocity showing a linear relation with a corresponding correlation coefficient $r = 58$ % well above the 99.9 % significance level. This implies that wind shears play an important role in the turbulence generation in the troposphere and lower stratosphere (through the Kelvin–Helmholtz instability).

Keywords. Meteorology and atmospheric dynamics (middle atmosphere dynamics; turbulence; waves and tides)

1 Introduction

Turbulence is an essential atmospheric motion over a wide range of length scales and timescales. It plays an important role in determining the evolution and structure of the free atmosphere as well as the trace gases and pollutants in it; this role is, however, far from being fully understood (e.g. Wyngaard, 1992; Lübken, 1992; Fritts et al., 2003, 2016; Müllemann et al., 2003; Sharman et al., 2012). The physical nature of turbulence is dissipative. It transfers energy from medium spatial scales to small scales, where the energy is converted to heat due to viscous dissipation. Turbulence has important effects on the thermal and dynamical structure of the atmosphere, the mixing of atmospheric constituents, and the stratosphere–troposphere exchange. In addition, clear-air turbulence (CAT) in the upper troposphere and lower stratosphere (UTLS) regions is a well-known threat to the safety of aviation (e.g. Sharman et al., 2011). Because of

the importance of turbulence in the atmosphere, theoretical and experimental efforts have been carried out to identify the turbulence generation mechanisms that remain a major concern of research to date. Previous studies show that the Kelvin–Helmholtz instability has long been recognized as an important source of turbulence (e.g. Klostermeyer and Rüster, 1980; Mega et al., 2010; Fritts et al., 2003). Convectively generated gravity waves and gravity wave breaking are also important causes responsible for turbulence generation (e.g. Lindzen, 1981; Fritts et al., 2003; Achatz, 2007). Furthermore, the remaining well-known generation mechanisms of turbulence include strong wind shears associated with jet streams and upper-level fronts, wave–wave interaction, mountain waves, convective clouds, and thunderstorms (e.g. Pantley and Lester, 1990; Pavelin and Whiteway, 2002; Fritts and Alexander, 2003; Sharman et al., 2012; Zovko-Rajak and Lane, 2014; Lane and Sharman, 2014).

Atmospheric turbulence is normally characterized by the energy dissipation rate ε. It is defined as the rate at which the amount of turbulence kinetic energy (TKE) is dissipated into heat by viscous forces at the Kolmogorov scale. Various techniques have been put forward to obtain ε from the experimental data, including in situ rocket, aircraft, and balloon-borne instruments (including radiosondes) (e.g. Lilly et al., 1974; Lübken et al., 1987; Schumann et al., 1995; Clayson and Kantha, 2008; Haack et al., 2014) as well as the Doppler lidars (e.g. O'Connor et al., 2010) and radars (e.g. Hocking, 1983, 1985; Nastrom and Eaton, 1997).

Triggered by the pioneering work by Woodman and Guillen (1974), ground-based radars (operating at frequencies from MF to UHF) were developed to monitor turbulence in the atmosphere due to their high temporal and spatial resolutions (e.g. Nastrom and Eaton, 1997). There are basically two parameters used to infer information for turbulence from the backscattered radar signals, i.e. the volume reflectivity (calibrated backscattered power) and the Doppler spectral width. Both methods are based upon the fact that turbulence causes fluctuations in the radar refractive index, which is determined by density, temperature, and humidity in the UTLS regions. On one hand, these fluctuations lead to detectable volume scatter; on the other hand, the underlying velocity fluctuations lead to a spectral broadening. Please note that both methods assume that atmospheric turbulence is isotropic and within the inertial subrange (i.e. turbulence is well developed). In the case of mesosphere–stratosphere–troposphere (MST) radars, the so-called "width" method has been put into use widely. This is based on the fact that the width of the Doppler spectrum due to atmospheric motions contains information about the intensity of atmospheric turbulence in the probing volume of radar. As specified by Hocking (1985) and Nastrom and Eaton (1997), the observed spectral width contains contributions due to turbulence as well as non-turbulent effects such as beam, shear, and wave broadening. In order to derive turbulent energy dissipation rates these contributions must first be subtracted quadratically from the observed spectral widths.

MST radars have been widely used to study turbulence in the lower and middle atmosphere based on the conversion of spectral width to the dissipation rate ε (e.g. Hocking, 1983, 1985; Nastrom and Eaton, 1997; Engler et al., 2005). The reliability of the radar measurements can usually be validated by comparison with similar observations with the right order of magnitude of the derived turbulence parameters. Although a few case studies have been put forward to directly compare radar measurements with in situ measurements by balloon (Zink et al., 2004; Kantha and Hocking, 2011), further studies are highly desirable. In this study, we compare radar-based estimates of ε (based on the Middle Atmosphere Alomar Radar SYstem – MAARSY – spectral width data) with radiosonde data applying a so-called Thorpe analysis (Thorpe, 1977; Clayson and Kantha, 2008; Wilson et al., 2011). These radiosonde measurements were obtained during the WADIS sounding rocket campaign in 2013 as described in Strelnikov et al. (2014). We are hence able to validate the radar estimates of turbulence by comparing them with the simultaneous in situ measurements with radiosondes. In Sect. 2 we describe the radar system of MAARSY and the experimental set-up and observations. In Sect. 3 we outline the methods to infer the turbulent energy dissipation rate from radar and radiosondes and present the comparison between the two techniques as a validation for each other. A preliminary climatology of turbulence from the MAARSY radar measurements is given in Sect. 4, which is then discussed in Sect. 5, in which we compare the derived dissipation rate with the background conditions. Finally, our conclusions are summarized in Sect. 6.

2 Observations

The MST radar echoes are caused by scattering or reflection from irregularities of the atmospheric refractive index. Details of these mechanisms are described by, for example, Gage and Balsley (1980), Gage et al. (1981, 1985), Hocking (1985), and Röttger and Larsen (1990). For monostatic radars, backscatter arises from refractive index variation Δn at the radar half wavelength (i.e. Bragg condition for monostatic radars: ~ 3 m for typical VHF radars). The n variations in the atmosphere are directly related to variations of the atmospheric parameters: humidity, temperature, pressure (corresponding to air density), and electron density. It has been demonstrated in many experimental studies that the MST radar echo power P_r is proportional to the generalized refractive index gradient squared M^2 when using a vertically directed radar beam (e.g. Hocking, 1985; Rapp et al., 2008). For a given radar operating at a fixed range resolution and with a fixed peak transmitter power, this relationship can be simplified as

$$P_{\mathrm{r}} \propto \frac{M^2}{z^2} \equiv \left(\frac{\mathrm{d}n}{\mathrm{d}z}\right)^2 \Big/ z^2. \quad (1)$$

According to Ottersten (1969), in the troposphere the generalized refractive index gradient M is defined as

$$M = -77.6 \times 10^{-6} \frac{p}{T}\left(N^2 + 15\,600 \frac{q}{T}\frac{N^2}{g} - \frac{7800}{T}\frac{\mathrm{d}q}{\mathrm{d}z}\right), \quad (2)$$

where N is the Brunt–Väisälä frequency, T the temperature, p the air pressure, q the specific humidity, and g the acceleration due to gravity (Tatarskii, 1961; VanZandt et al., 1978). The first term on the right side is called the dry term and the second and third terms indicate the influences of q and $\mathrm{d}q/\mathrm{d}z$, respectively.

MAARSY is a monostatic radar operating at a frequency of 53.5 MHz in coherent scatter mode (Latteck et al., 2010). The radar system is an active phased array consisting of 433 linearly polarized Yagi antennas where each element is connected to an individual transceiver module with high flexibility in phase control and power output. The power transmission of each element of up to 2 kW peak gives a maximum peak power of $\sim$ 866 kW. The design of a nearly circular array results in a very symmetric radiation pattern with a one-way full beam width of 3.6° at half power corresponding to a diameter of $\sim$ 630 m at an altitude of 10 km. MAARSY can be steered with zenith angles down to 30°. The radar system is located at Andøya, Norway (69.03° N, 16.04° E) and designed for studying polar atmosphere, i.e. the UTLS (the upper troposphere and lower stratosphere) and MLT (the mesosphere and lower thermosphere) regions covering the ionospheric E region altitudes in polar regions (Rapp et al., 2011; Renkwitz et al., 2012, 2013; Stober et al., 2012, 2013; Chau et al., 2014; Latteck and Strelnikova, 2015). The basic parameters of the radar system are summarized in Table 1 for convenience. For more details on the technical description of MAARSY, the reader is referred to Latteck et al. (2010, 2012).

The data sets presented in this study were obtained with MAARSY for tropospheric experiments during the period of 2010–2013 (a total of 522 days) consisting of three sequences based on different experimental configurations. The data acquisition and data analysis of raw data were routinely carried out with a commercial software package. The histogram in Fig. 1 shows the distribution of data sets in different months. The recorded complex raw data (I and Q) are time series with a typical data length of 256 or 512 points. The data with some coherent integrations (CI; ranging between 64 and 526 CI) have been used for estimating the autocorrelation functions (ACFs) which according to the Wiener–Khinchin theorem are the Fourier transforms of the power spectra. For the case of coherent scatter (e.g. scattering from turbulent structure), a Gaussian shape of the spectrum is assumed, which is valid for the here used data. The magnitude

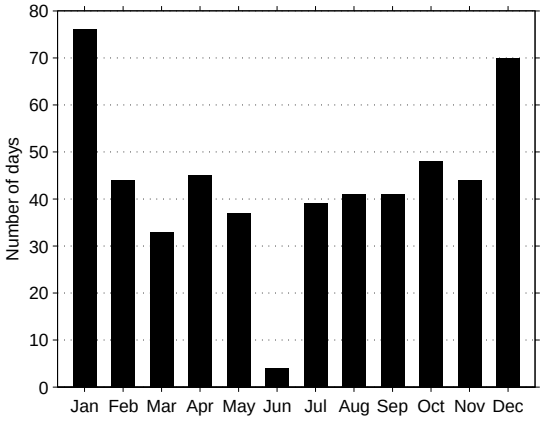

Figure 1. Length of data set in different months available for the current study during the period of 2010–2013.

of the ACF can be approximated as (Strelnikova and Rapp, 2011)

$$\mathrm{ACF}(\tau) = \mathrm{ACF}_{\tau=0} \cdot \exp\left\{-(\tau/\tau_e)^2\right\}, \quad (3)$$

where ACF is the magnitude of the autocorrelation function, τ the time lag at which the ACF is evaluated, and τ_e is a correlation time (or decay time which is inversely related to the spectral width). After fitting the measured ACF magnitude to the above function, the correlation time τ_e and hence the half width at half maximum (HWHM) of the Gaussian function were determined according to the following relationship

$$\mathrm{HWHM} = \sqrt{\ln 2} \cdot \frac{1}{\pi\,\tau_e}. \quad (4)$$

Then the experimental spectral width ω_{obs} (in $\mathrm{m\,s^{-1}}$) can be determined as $\omega_{\mathrm{obs}} = \mathrm{HWHM} \cdot \lambda/2$ and recorded, where λ is the radar wavelength (5.6 m for MAARSY). In the calculation the ACFs with a signal-to-noise ratio (SNR) smaller than 3 dB are not included in further analysis. Furthermore, a procedure to disregard the regions around the sea clutter frequencies is included in the calculation. The short-term events including aircrafts, meteors, etc., however, are carefully rejected by considering SNR values; i.e. data with unpredictably large SNR are rejected. Finally, the best Gaussian fittings were carefully derived to ensure that the ACFs showing other strange properties are not accepted.

MAARSY has the capacity to steer the beam on a pulse-to-pulse basis allowing us to measure the radial velocities for several different beam directions in one experiment. Here we make use of the Doppler beam swinging (DBS) technique to estimate horizontal wind fields (both zonal and meridional) from five beams (one in the vertical direction and four at an off-zenith angle of 10° in orthogonal azimuths) with a temporal resolution of 5 min. The wind observations were estimated based on a single-cycle set-up, which permits us to derive complete wind information after

Table 1. Basic parameters of MAARSY.

	Description
Location	Andøya, Norway (69.03° N, 16.04° E)
Operating frequency	53.5 MHz
Allocated bandwidth	4 MHz
Peak power	866 kW
Maximum duty cycle	5 %
Pulse repetition frequency	≤ 30 kHz
Pulse length	≥ 0.33 µs
Sampling resolution	≥ 50 m (300 m in the current study)
Transmitted waveforms	single pulse, complementary and Barker codes
Pulse shapes	square, Gaussian, shaped trapezoid
Antenna type	three-element Yagi
No. of antennae	433
Effective antenna area	$\sim 6300\,\mathrm{m}^2$
Half power full beam width (one way)	3.6° (~ 630 m at an altitude of 10 km)
Directive gain	≤ 33.5 dBi
Beam directions	arbitrary at zenith angles $< 30°$
Receiving channels	16

the experiment running time (e.g. Röttger and Larsen, 1990; Stober et al., 2012, 2013). The spectral widths derived in the vertical beam were utilized to infer ε since the effects of beam broadening are smallest for the vertical geometry compared to the oblique beams.

Figure 2 shows examples of the radar echo power with MAARSY and the squared Brunt–Väisälä frequency N^2 calculated based on the temperature from the ECMWF reanalysis data as well as horizontal winds and spectral widths from the radar measurements with MAARSY from top to bottom during a period of 28 days. Within the altitude range of 9–13 km, there are clearly enhancements in echo power, which took place just above the tropopause heights. The tropopause heights are determined based on the temperature profiles taken from the ECMWF reanalysis data: the lapse rate tropopause (LRT) is shown in red and the cold point tropopause (CPT) in black. The values of N^2 indicating static stability of the atmosphere in the second panel from top show nearly constant values in the troposphere and lower stratosphere, i.e. $N^2 = 1 \times 10^{-4}\,\mathrm{s}^{-2}$ in the troposphere and $N^2 \geq 4 \times 10^{-4}\,\mathrm{s}^{-2}$ in the lower stratosphere. Furthermore, N^2 profiles reveal a sharp increase by a factor of 4 or more in the magnitude just above the tropopause which reveals the existence of the so-called tropopause inversion layer (TIL) (see Birner, 2006, for details) and has nearly constant values in the stratosphere above the layer. The comparison between echo power and N^2 reveals a clear correlation. In the UTLS regions where humidity can be neglected, M is conveniently approximated by the dry term (see Eq. 2). Therefore, M is proportional to N^2 and to p/T. As mentioned above, the term p/T is directly dependent on the air density, $p/T \propto \rho_0 \exp(-z/\overline{H})$, where ρ_0 is the density at mean sea level and $\overline{H}$ the mean scale height across the considered altitude range. Inserting these relationships into Eq. (1), we finally reach a simplified expression:

$$P_\mathrm{r} \propto \frac{[\exp(-z/\overline{H})N^2]^2}{z^2}; \tag{5}$$

i.e., the enhanced echoes at vertical incidence often measured with VHF radars at or above the tropopause are determined by variations of the N^2 profiles. The MST radar measurements hence provide a measure of the background static stability (N^2) which has been widely used for studying various atmospheric properties such as the estimate of the tropopause height (e.g. Gage and Green, 1982; Hall et al., 2009), tropopause folds and meteorological fronts (e.g. Röttger, 1979; Larsen and Röttger, 1983; Bertin et al., 2001; Mihalikova et al., 2012). Furthermore, the minima of echo power occurred just below the tropopause where the convective fluctuations cease. There are strong wind fields (to be specific, $U > 20\,\mathrm{m\,s}^{-1}$) with maxima up to more than $\sim 55\,\mathrm{m\,s}^{-1}$ occurring in the altitude range of 8–11 km, generally below the tropopause. The observed spectral widths show a similar structure compared with the background horizontal winds.

3 Methodology

In this section, the ε analysis based on radar- and radiosonde observations is described.

3.1 Derivation of ε with radar

There are several ways to derive estimates of the turbulent energy dissipation rate from clear-air radar observations. These

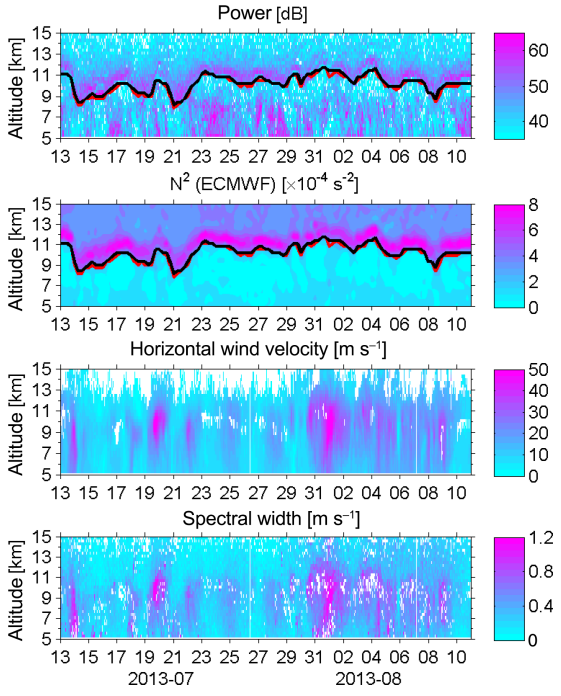

Figure 2. Height–time cross sections of echo power from the radar measurements with MAARSY and temperature derived from the ECMWF reanalysis data as well as horizontal winds and spectral widths with MAARSY from the uppermost to lowermost panels, respectively, during the period of 13 July–10 August 2013. The lines (in the upper two panels) indicate the tropopause height according to temperature profiles from ECMWF: red line for lapse rate tropopause (LRT) and black for cold point tropopause (CPT).

methods include ε estimates from the structure constant C_n^2, which may be derived from calibration observations of the radar signal strength and the width of the observed Doppler spectrum (e.g. Hocking, 1985). However, the conversion of C_n^2 to ε needs several assumptions (e.g. Lübken, 1992). In this study, we make use of the measurements of spectral width to estimate ε.

Spectral widths have been estimated from the correlation time τ_e as described above. Before taking a step further, we should note that a finite beam width leads to a number of broadening effects on the spectral width observed in coherent scatter observations (e.g. Hocking, 1985; Murphy et al., 1994; Nastrom and Eaton, 1997). The correction of these broadening effects may be comparable or even larger than the spectral broadening due to turbulence and must be carefully removed from the observed spectral widths. The observed spectral width ω_{obs} is actually the sum of different terms, i.e.

$$\omega_{\text{obs}}^2 = \omega_{\text{turb}}^2 + \omega_{\text{beam}}^2 + \omega_{\text{shear}}^2 + \omega_{\text{wave}}^2, \quad (6)$$

where ω_{turb} is the contribution from turbulent velocity fluctuations in the medium, ω_{beam} is the contribution from beam broadening, ω_{shear} is the contribution from shear broadening, and ω_{wave} is the contribution from high-frequency gravity waves. Note, the gravity wave correction in the lower atmosphere is usually relatively small compared with the other corrections (e.g. Murphy et al., 1994) and is hence ignored in the current study; i.e. $\omega_{\text{obs}}^2 = \omega_{\text{turb}}^2 + \omega_{\text{beam}}^2 + \omega_{\text{shear}}^2$. In addition, physically realistic values of ω_{turb}^2 must be positive. However, the actual values of turbulence intensity are often very near zero (Schumann et al., 1995) and the corrections are sometimes larger than ω_{obs}^2 due to sampling errors and statistical fluctuations leading to estimates of $\omega_{\text{turb}}^2 < 0$, especially under strong wind conditions such as in the presence of a jet stream (e.g. Dehghan and Hocking, 2011). In the subsequent calculation we hence only use the positive values of ω_{turb}^2. According to Hocking (1985), the beam broadening contribution may be quantified as $\omega_{\text{beam}} = \frac{1}{2\sqrt{2}} \cdot \vartheta \cdot V$, where ϑ is the 3 dB full beam width of the transmitted radar beam (in radian) and V the horizontal wind velocity. Expressions for shear broadening are given, for example, by Nastrom and Eaton (1997) and can be written as $\omega_{\text{shear}} = \vartheta/6 \cdot \mathrm{d}V/\mathrm{d}z \cdot \Delta R$, where ΔR is the length of a range gate (300 m for the current study). From the derived ω_{turb}^2, the turbulent energy dissipation rates ε can then be determined based on the following relation (Hocking, 1985):

$$\varepsilon = \frac{0.4\omega_{\text{turb}}^2 N}{2\ln 2}, \quad (7)$$

where N is the Brunt–Väisälä frequency, which is here taken from the ECMWF reanalysis data.

In the left two panels of Fig. 3 we show vertical profiles of the observed spectral width (ω_{obs}^2 in blue) and the corrected spectral width after removing the broadening effects (ω_{turb}^2 in red) and the vertical shears of horizontal wind derived from radar observations with MAARSY over the period of 1 h, straddling the time of the radiosonde flight, which began at 16:12 UTC on 29 June 2013. The squared Brunt–Väisälä frequency N^2 derived from the ECMWF reanalysis data averaged for 1 day on 29 June 2013 is shown in the third panel from left. Finally, the calculated turbulent energy dissipation rates (the means and standard deviations) based on Eq. (7) are shown in the right-most panel. ω_{obs}^2 show values much larger than ω_{turb}^2 (twice the value or more). The profiles of ω_{obs}^2 show an increase in the troposphere and decrease in the stratosphere, i.e. maximizing near the tropopause, while ω_{turb}^2 shows a clear peak just below 11 km which reflects a significant turbulent layer. The derived ε profile in the right-most panel shows a nearly constant value in troposphere and stratosphere and an enhancement near the tropopause (just below 11 km). There is a positive correlation between the derived ε and the corresponding wind shears. Furthermore, there are significant turbulent layers occurring below 11 km in the regions with large N^2 values, whereas there are no layers between 7 and 8 km, where even wind shears were strong. This appears to be due to their dependence on N according

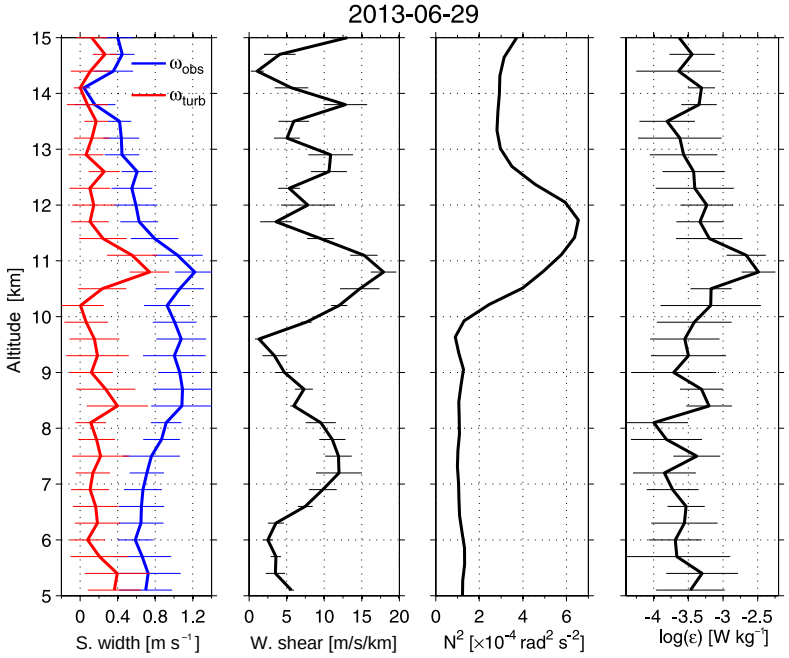

Figure 3. Profiles of spectral width (ω_{obs} and ω_{turb}), wind shear derived from radar observations with MAARSY, and turbulent energy dissipation rate converted from ω_{turb}(mean values and standard deviations) over the period of 1 h, straddling the time of the radiosonde ascent on 29 June 2013 (the flight began at 16:12; see Fig. 4) in the first, second, and fourth panel from left, respectively, and the squared Brunt–Väisälä frequency (N^2) derived from the ECMWF reanalysis data averaged over 1 day on 29 June 2013 in the third panel from left.

to Eq. (7). The discussion of this correlation will be carried out in more details in Sect. 5.

The data presented here were analysed with a commercially available software package, which does not provide statistical uncertainties to the estimated parameters, i.e. the spectral width or radial velocity. As already described, these parameters are derived from the ACF of the measured time series. Typically 256 or 512 points are recorded after some coherent integrations (CI), which range between 64 and 256 CI for the data analysed here. In order to obtain an estimate of the statistical uncertainties, we applied a more sophisticated approach by fitting a truncated Gaussian to the measured spectra. The fitting routine is based upon the concept presented in Kudeki et al. (1999), Sheth et al. (2006), and Chau and Kudeki (2006). This spectral Gaussian fitting takes into account the effects of the rectangular window and the temporal sampling. We estimated the statistical uncertainties after applying additional incoherent integrations (of 4, 8, and 16) to the time series. The error distribution looks like a Poisson distribution for the radial velocities with a peak at 8–12 cm s^{-1} as well as for the spectral widths, with a long tail towards larger values. The largest errors are typically associated with low SNR values. However, as the spectral domain fitting applies additional incoherent integrations, it is possible to obtain successful fits with SNR > -8 dB. However, as most of the analysis was conducted in the ACF domain, there might be differences between the statistical uncertainties in both approaches, in particular, for low SNR values at SNR < 3 dB (ACF domain). Hence, all SNR values below this threshold are disregarded. The threshold of 3 dB in the ACF domain is associated with errors of about 20 cm s^{-1} in the spectral domain. This may still lead to large uncertainties in the derived ε even at $\varepsilon_{error} > \varepsilon$. The estimated error, however, represents a maximum uncertainty by conducting full error propagation. The huge number of measurements with reasonable ε values suggests that the error is likely much smaller.

3.2 Derivation of ε from radiosonde data

During the WADIS sounding rocket campaign in 2013 (Strelnikov et al., 2014), there were 14 launches of balloon-borne radiosondes (model: MarkIIa DGPS (LOS), (p/n 1648–611)) at the radar site of MAARSY. The ascent rate of the radiosondes (RS) used in this study was roughly 5 m s^{-1}. They had a temporal resolution of 1 s corresponding to a 5 m height resolution. Most of the launches were carried out during the period from 16:00 to 24:00 UTC, with one flight after local noon and one shortly after midnight. All the RS soundings cover the altitudes from the atmospheric boundary layer (ABL) up to 25 km and/or beyond. Some sondes contained a few bins with missing data, which were filled by linear interpolation.

Meteorological RS provide measurements of pressure (P in hPa), temperature (T in K), relative humidity (RH in

Table 2. Basic information of the 14 radiosondes including the launch and end times (UTC), the maximum height (m), the simultaneous radar measurements for comparison, and the measurement noise (mK).

No.	Sonde ID	Start	End	Max. h. (m)	Radar obs.	σ_θ (mK)
01	27061304	17:35:58	19:13:44	27 223	no	47.5
02	27061305	20:18:43	21:26:41	24 233	no	50.4
03	27061306	22:37:12	00:16:18	25 069	no	43.2
04	27061307	00:25:46	02:40:49	26 306	no	52.8
05	28061301	13:53:59	15:11:58	26 843	no	53.2
06	28061302	16:12:41	17:26:27	26 578	yes	64.4
07	29061301	16:12:55	17:23:49	25 790	yes	50.2
08	29061302	17:31:34	19:47:59	26 529	yes	51.5
09	30061301	16:15:05	18:38:58	27 427	yes	55.2
10	30061302	17:55:02	19:02:26	25 694	yes	56.4
11	30061303	20:11:00	22:57:38	27 053	yes	41.3
12	01071301	16:20:13	17:27:01	25 696	yes	53.9
13	01071302	17:41:59	19:24:23	34 788	yes	85.5
14	01071303	20:19:36	21:28:48	25 666	yes	53.8

%), and horizontal wind components. From the observations, potential temperature profiles are inferred from the relation

$$\theta = T\left(\frac{1000}{P}\right)^{R/c_p}, \tag{8}$$

where R is the specific gas constant of dry air, c_p the specific heat capacity, and $R/c_p = 0.286$ for air. If the potential temperature is monotonically increasing with altitude, the atmosphere is statically stable. This is mostly the case. Regions with negative θ gradient are statically unstable. Such overturns are indicative of turbulence. Following this idea, Thorpe (1977) developed a concept to indirectly measure turbulent energy dissipation rates ε by detecting static instabilities in oceans and lakes; this concept was adapted to the atmosphere by Luce et al. (2002) and Clayson and Kantha (2008).

The Thorpe analysis consists of rearranging an observed profile of potential temperature θ into a monotonically increasing one by sorting the order of data points upwards or downwards. The vertical displacements D_T needed for the sorting process are called *Thorpe displacements*. Specifically, if an air parcel at altitude z_n is moved to z_m, the resulting Thorpe displacement at z_n is $D_\mathrm{T}(z_n) := z_n - z_m$. The root mean square of the Thorpe displacement over an overturn is the *Thorpe length*, i.e. $L_\mathrm{T} := \mathrm{rms}(D_\mathrm{T})$. It is a measure of the vertical distance where heavier air is above lighter air. Thorpe (1977) proposed it to be a measure of the outer vertical scale of turbulence. Thus he assumed in a statistical way a proportionality of the Thorpe length L_T to the *Ozmidov length scale* $L_\mathrm{O} := \alpha\left(\varepsilon/N^3\right)^{1/2}$, where N is the Brunt–Väisälä frequency and α is a constant near unity, i.e. $L_\mathrm{O} = cL_\mathrm{T}$ with an empirical constant c. In particular, he uses quantities "averaged over many profiles which are supposed statistically similar and averaged over some vertical scale exceeding [the Thorpe displacement]" (Thorpe, 1977). Dillon (1982) infers a proportionality between L_T and L_O from the turbulent energy budget by using some assumptions. This relationship has been extensively studied and confirmed in the ocean in both observations and laboratory experiments, although the values of c involve some uncertainty with a broad value range (e.g. Dillon, 1982; Wesson and Gregg, 1994; Thorpe, 2005). Further studies also show that the values of c may depend on the measurement location and show variability with time (e.g. Yagi and Yasuda, 2013; Mater et al., 2013). Some studies in the atmosphere also exist (Gavrilov et al., 2005; Wilson et al., 2014; Schneider et al., 2015). From the proportionality between L_T and L_O, one obtains for the determination of dissipation rates

$$\varepsilon = C_\mathrm{K} L_\mathrm{T}^2 N^3, \tag{9}$$

where $C_\mathrm{K} = c^2$. The estimate of C_K is key for the Thorpe analysis to determine dissipation rates. In the case of ocean, it is usually found from in situ experiments that $C_\mathrm{K} \approx 1$. However, there are only few examinations of C_K for the atmosphere. For example, $C_\mathrm{K} = 1.15$ was used by Gavrilov et al. (2005). Clayson and Kantha (2008) analysed radiosondes by applying $C_\mathrm{K} = 0.3$ taken from oceanic measurements while Kantha and Hocking (2011) inferred $C_\mathrm{K} = 1$ by a comparison of radiosonde and radar measurements. The variability in C_K is also due to the fact that the values of this ratio depend on the degree of the development of turbulence, and $C_\mathrm{K} \approx 1$ only when turbulence is fully developed (Gavrilov et al., 2005; Kantha and Hocking, 2011). Schneider et al. (2015) used a balloon-borne Leibniz Institute Turbulence Observations in the Stratosphere (LITOS) instrument to derive ε which is independent of L_T. The ratio of $L_\mathrm{O}/L_\mathrm{T}$ shows a large variability of values, with the full width at half maximum spanning ~ 1.9 orders of magnitude. Recently, Fritts et al. (2016) employed direct numerical simulation (DNS) on

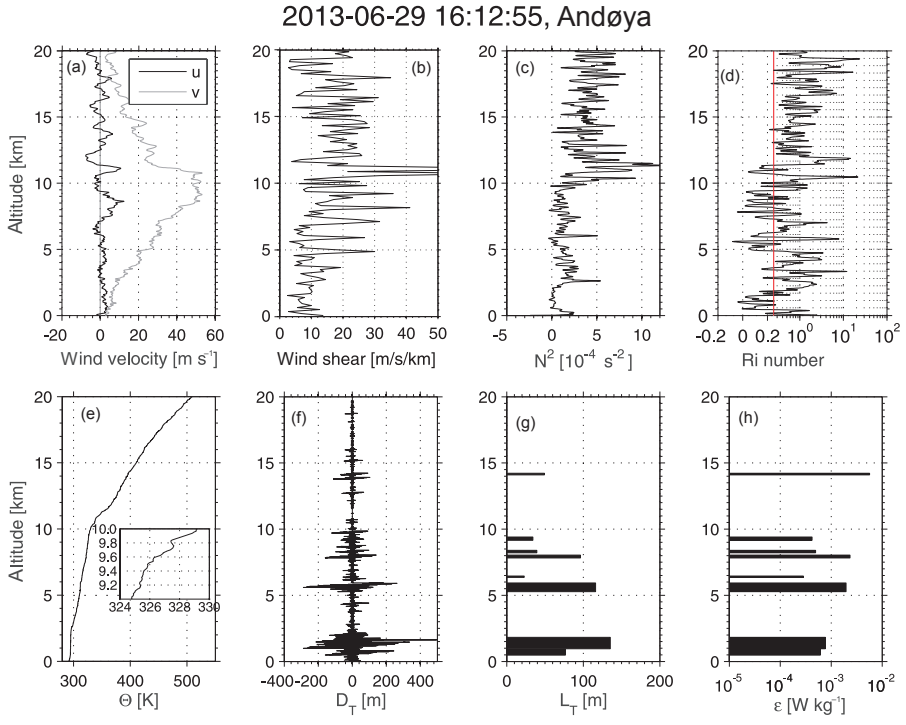

Figure 4. Vertical profiles of the atmospheric parameters inferred from the radiosonde on 29 June 2013 at Andøya: **(a)** velocity of zonal wind u (black) and meridional wind v (blue), **(b)** vertical shear of horizontal wind, **(c)** Brunt–Väisälä frequency squared (N^2), **(d)** Richardson number calculated based on a height resolution of 150 m and the red line indicating $Ri = 1/4$ (see text for details), **(e)** moist-conservative potential temperature (i.e. including the effects of air moisture), **(f)** Thorpe displacement (D_T), **(g)** Thorpe length (L_T), and **(h)** the derived energy dissipation rate ε based on Thorpe analysis.

multiscale dynamics to assess the relation $c = L_\mathrm{O}/L_\mathrm{T}$. They found that the c values are highly variable with event type and time and tend to increase with time. Based on event type and character, a mean c can be defined with suitable averaging, for example, $c \approx 0.8$–1 derived from ~ 12 to $20T_\mathrm{b}$ (where T_b is buoyancy period). This issue should be studied further with more simultaneous measurements with more than two instruments in the future. In this study, $C_\mathrm{K} = 1$ is used following Kantha and Hocking (2011).

The analysis in this study is performed according to Wilson et al. (2011). First, pressure is smoothed with a spline fit to be monotonically decreasing, and all data are resampled to have a constant altitude increment. Moisture is handled as suggested by Wilson et al. (2013); i.e. moist regions are detected, and within these the moist potential temperature is used instead of the dry one. Then the sorting is performed and the Thorpe displacements D_T are computed. The cumulative Thorpe displacements are defined by the cumulative sum of the Thorpe displacement, $C_\mathrm{T}(k) := \sum_{i=0}^{k} D_\mathrm{T}(i)$. Inversions are identified by regions with negative cumulative Thorpe displacements C_T. The idea is that for stable regions C_T is zero as the potential temperature is already sorted. Instrumental noise is an important issue, because it can create artificial inversions. Wilson et al. (2010) introduced a statistical test to select real overturns and reject inversions created by noise. It consists of comparing the range of the potential temperatures within an inversion to the range of a pure noise sample of the same length and given standard deviation σ_θ. Wilson et al. (2011) proposed a simple method to compute the measurement noise σ_θ from the radiosonde data itself, which is applied in this study. Basically, the temperature profile is split into segments of 200 m altitude, and in each segment, the noise standard deviation of the temperature σ_T is set to the standard deviation of the first differences of the data after trend removal divided by $\sqrt{2}$. σ_θ is then computed with Gauss' law of error propagation, neglecting the error in pressure because it is much smaller than that of the temperature. For each significant overturn, the Thorpe length L_T is calculated. Thereby, with a mean buoyancy frequency $\overline{N}$ in the layer, the energy dissipation rate ε is obtained via Eq. (9). The Brunt–Väisälä frequency N is computed from the sorted θ profile, and a Hann-weighted smoothing over 31 data points (roughly 150 m altitude) is applied to θ before numerical differentiation to prevent the derivative to be dominated by instrumental noise.

The basic information of the 14 radiosondes including measurement noise is listed in Table 2.

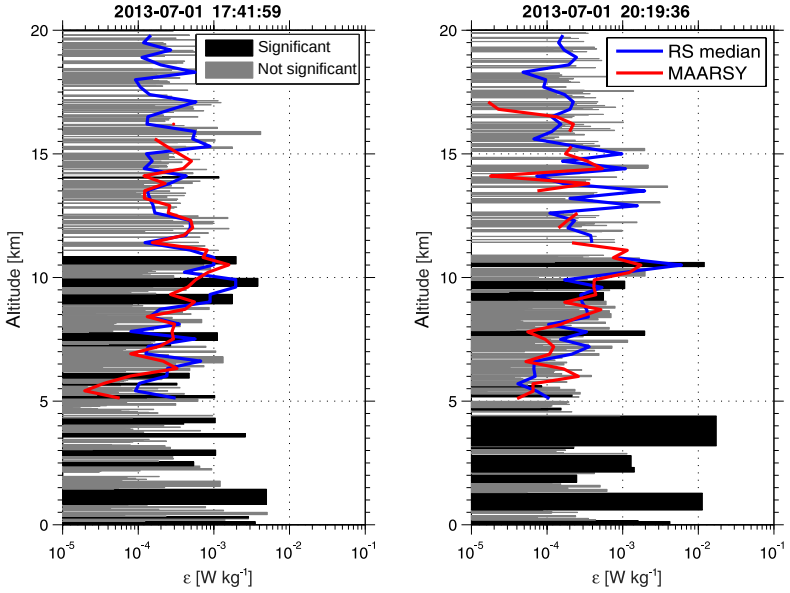

Figure 5. Vertical profiles of the derived dissipation rates from radiosondes (significant layers in black and non-significant layers in grey) with the median profile (in blue) and from radar (in red). Here all turbulent layers, including both significant and non-significant ones, from radiosondes were calculated as median for the comparison with the radar results. Please note the different height resolution of both instruments: 5 m for radiosondes and 300 m for radar. In order to compare the radar and radiosonde values one-to-one, we infer the median of radiosonde ε over 300 m consistent with the height resolution of radar measurements, and they are shown in blue. The radar ε is calculated as the median for the period of 2 h, straddling the time of the radiosonde ascent (two flights on 1 July 2013).

In Fig. 4a–h, we show an example of vertical profiles of the atmospheric parameters inferred from the balloon-borne radiosonde on 29 June 2013. Vertical profiles of wind velocities in Fig. 4a show much weaker zonal winds than meridional winds, with zonal winds generally less than $10\,\mathrm{m\,s^{-1}}$. The vertical shears of horizontal wind $S = \sqrt{(\mathrm{d}u/\mathrm{d}z)^2 + (\mathrm{d}v/\mathrm{d}z)^2}$ are calculated and shown in Fig. 4b. The squared Brunt–Väisälä frequency (N^2) in Fig. 4c shows nearly constant values of $1.0 \times 10^{-4}\,\mathrm{s^{-2}}$ in the troposphere (below 10 km) and of $4.0 \times 10^{-4}\,\mathrm{s^{-2}}$ in the stratosphere. The so-called tropopause inversion layer (TIL) with a jump in the N^2 profile of up to more than $10.0 \times 10^{-4}\,\mathrm{s^{-2}}$ is seen at 11 km (e.g. Birner, 2006). The Richardson number Ri defined as the ratio of the squared Brunt–Väisälä frequency to the squared wind shear is calculated with a height resolution of 150 m and shown in Fig. 4d. In Fig. 4e we show the potential temperature calculated by taking into account the effects of air moisture. As shown by Wilson et al. (2013) such effects on turbulence detection can be dramatic for a cloudy or moist atmosphere (saturated with water vapour). Hence, the moist potential temperature is used for further calculation in this study. The θ profile generally reveals a gradual increase up to 11 km (near the tropopause) and a more steeper increase thereafter. However, a magnified part from 9.0 to 10.0 km is shown in the inset for a better visibility of the negative gradients of θ, indicative of turbulent eddies. After rearranging the θ profile with overturns into a stable monotonic profile, the Thorpe displacements are derived and shown in Fig. 4f. Note that only significant overturns were selected as described above. The Thorpe length L_T defined as the root mean square (rms) of D_T is shown in Fig. 4g. Finally, the turbulent energy dissipation rates ε are determined from the Thorpe length and the Brunt–Väisälä frequency measured with the radiosonde according to Eq. (9) and shown in Fig. 4h. The Richardson number is an important parameter to characterize the stability of the atmosphere. According to linear theory, the atmosphere tends to lead to the occurrence of turbulence when $Ri < Ri_\mathrm{c}$, where $Ri_\mathrm{c} = 1/4$ is the critical Richardson number (Miles, 1961). From our results, there is very strong turbulence at altitudes of, for example, 0.5–2.0 and 5.0–6.0 km, where Ri values are relatively small. By contrast, no turbulence or non-significant turbulence (not shown here) is found in the stratosphere where Ri values are larger ($> 1/4$). Further comparison between ε and Ri shows that there is a negative correlation between them, i.e. stronger ε detected in conditions with smaller Ri values. However, many experimental and theoretical studies reveal a more complicated and not a straightforward relation between turbulent flow and Ri_c (e.g. Achatz, 2007; Balsley et al., 2008; Haack et al., 2014).

3.3 Comparison of ε from both techniques

As mentioned above, the comparisons between the remote sensing observations with radar and the in situ measurements are desirable in order to ensure their reliability. With the si-

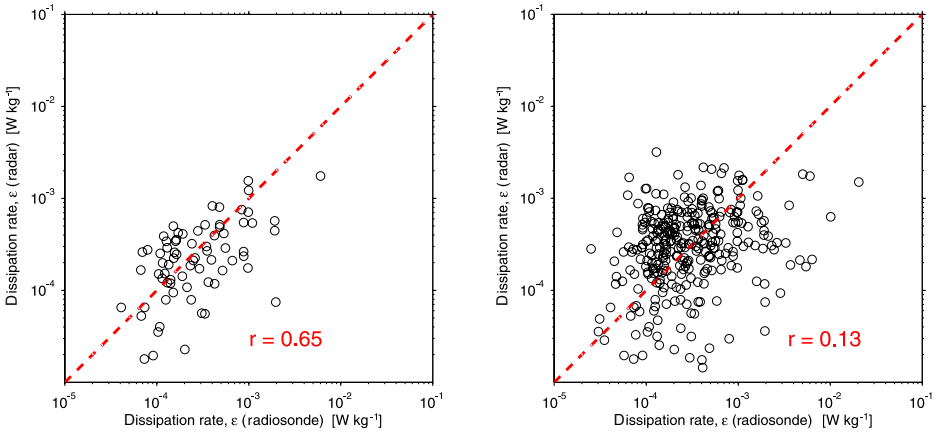

Figure 6. Scatter plots of the turbulent energy dissipation rates derived from the simultaneous measurements with radiosondes and radar. Left panel: the results derived based on the measurements during two flights on 1 July 2013 (i.e. the profiles shown in blue and red in Fig. 5). All turbulent layers, including both significant and non-significant ones, from radiosondes are included. The dashed line indicates an expected linear relation between them. In addition, we show the corresponding correlation coefficient $r = 0.65$, which is highly significant, i.e. well above the 99.9 % level. Right panel: the results derived from all the nine flights with the simultaneous measurements with MAARSY. Here, the corresponding correlation coefficient is at $r = 0.13$, which is not significant.

multaneous measurements of collocated radar and balloon-borne radiosondes in hand, we are able to validate the radar estimates of turbulent energy dissipation rate by a comparison between both techniques.

Before going into detail, we should note that the two instruments do not measure the same volume (i.e. they have a different horizontal coverage) and their height resolutions are quite different: 5 m for radiosondes and 300 m for radar. In Fig. 5 we show the altitude profiles of the ε values derived from radiosondes with the significant layers in black and non-significant layers in grey. In order to compare the radar and radiosonde values one-to-one, we calculate the median of radiosonde ε for all turbulent layers, including both significant and non-significant ones, over 300 m consistent with the height resolution of radar measurements. The radar ε are calculated as the median for a period of 2 h, straddling the time of the radiosonde ascent. Figure 5 shows the comparison of turbulent energy dissipation rates derived from radar and radiosonde measurements of two flights on 1 July 2013. The ε values derived from radiosondes up to $10^{-2}\,\mathrm{W\,kg^{-1}}$ cover several orders of magnitude, which indicates the large variability inherent in turbulent energy dissipation rates and highly intermittent characteristics of turbulence in the free atmosphere. Furthermore, there is an enhancement of ε below ~ 2 km, where there is the atmospheric boundary layer characterized by strong vertical mixing and strong turbulence. This property is also seen in other flights (not shown here). The medians of the radiosonde ε (in blue) show an overall agreement with the radar ε values, which, however, are the medians derived over a 2 h period.

We further show scatter plots of the derived ε one-to-one values and an identity line (dashed line) as a reference in Fig. 6. The ε values derived from all the simultaneous measurements with both instruments (shown in the right panel) fall within nearly the same range, although the 1 : 1 correlation is very weak. For the ε values derived during two flights on 1 July 2013 (shown in the left panel), however, the comparison shows a nearly linear correlation, with a highly significant correlation coefficient at $r = 0.65$, which is very encouraging. The correlations between the squared Thorpe length (L_T^2) and the squared spectral width due to turbulence (ω_turb^2) are further investigated in order to remove the involvement of the Brunt–Väisälä frequency in the estimate of ε for both techniques (see Eqs. 7 and 9, figure not shown here). The comparisons between them show that there is a significant correlation between both parameters for the measurements during two flights on 1 July 2013, whereas there is a less significant correlation for all the simultaneous measurements. This implies that the significant correlations of the ε values derived from both techniques are not due to the N term in Eqs. (7) and (9), although of course turbulence is related to the Brunt–Väisälä frequency which characterizes the convective or static stability of the atmosphere.

Given the large variability of turbulent energy dissipation rates and the difference between the two techniques (see the caveats mentioned above), the only fair method is to compare their statistical results. There are 9 flights of radiosondes out of 14 during the WADIS sounding rocket campaign in 2013 with simultaneous radar measurements. The histogram of the ε values derived from radiosondes as well as from radar (spanning in 2 h period as described above) for the same time and same altitudes is shown in Fig. 7 (left and middle panels). The histograms show similar properties of ε covering nearly the same range and peaking at almost the same value. We

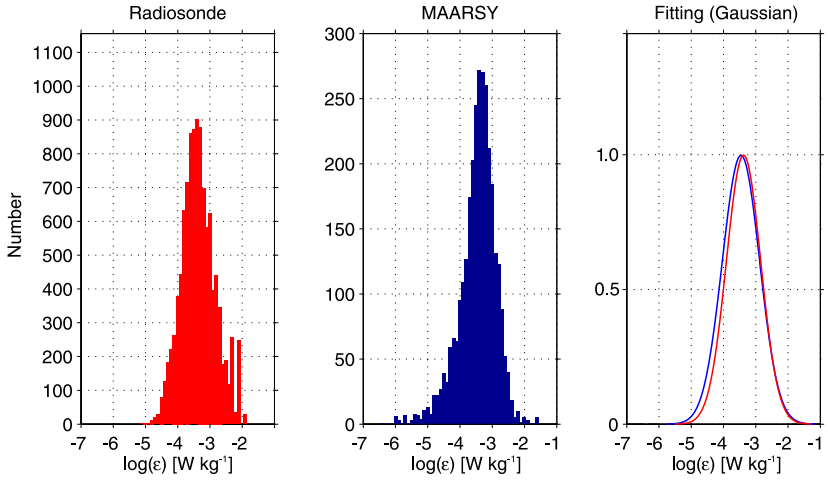

Figure 7. Histograms of the derived dissipation rates from radiosondes (left panel) and radar (middle panel) based on the simultaneous measurements during the WADIS campaign in 2013. All turbulent layers, including both significant and non-significant ones, from radiosondes are taken into account. In order to compare the ε distribution from both instruments, we fit the ε histograms with a Gaussian function, and the normalized fitting lines are shown in the right panel.

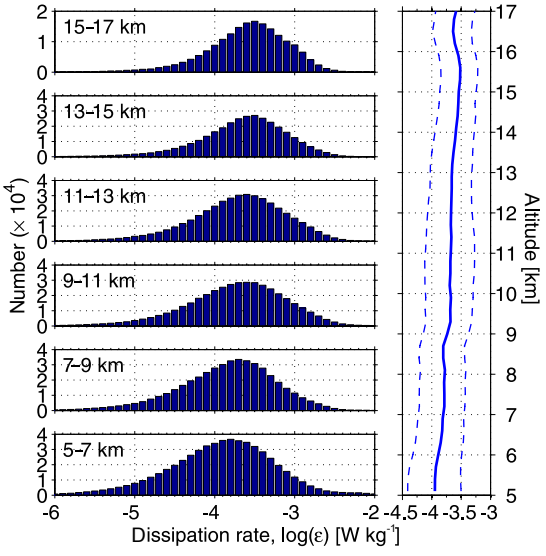

Figure 8. Histogram of the logarithm of the derived ε within the altitude ranges of 2 km each as well as the vertical profiles of the logarithm of the ε median (solid line) and the upper and lower quartiles (dashed lines) based on all 522-day radar observations with MAARSY during the period of 2010–2013.

note, however, that the full-width half-maximum amplitude of the distribution of the radiosonde ε is wider than the radar ε (by $\sim$0.3 order of magnitude). Further, we fit both histograms with a Gaussian function, and the normalized fitting lines are shown in the right panel of Fig. 7. The comparison of the fitting lines shows a very similar distribution of ε, although it seems that MAARSY can detect weaker turbulence than radiosondes.

In a nutshell, the comparison is very encouraging in that the derived ε display a linear correlation one-to-one with both techniques for individual cases and the statistical results. The histograms show the ε values falling within a similar range and with the largest numbers occurring at almost the same value. Hence, the comparison should be considered as a way to validate the derivation of turbulent energy dissipation rate from radar measurements based on the in situ measurements with balloon-borne radiosondes. Conversely, it also provides a method to calibrate the value of C_K used in Thorpe analysis.

4 Climatology of turbulence with radar

In this section, we apply the analysis described in Sect. 3.1 to all the data available to derive a preliminary climatology of turbulent energy dissipation rate ε. Figure 8 shows the derived ε as histograms for every 2 km from 5 up to 17 km as well as the vertical profile of the logarithmic ε median and the upper and lower quartiles derived from all the 522-day observations with MAARSY between 2010 and 2013 available for this study (cf. Fig. 1). The ε distributions show that energy dissipation rates fall within a range between 10^{-7} and 10^{-2} W kg^{-1}, covering 5 orders of magnitude. The ε distribution cannot be characterized by a Gaussian function but is approximately log-normal with a negative skewness as expected for intermittent turbulent flows (Nastrom and Gage, 1985; Nastrom and Eaton, 1997; Fritts et al., 2003; Frehlich et al., 2004). The ε medians (right panel in Fig. 8) show an increase with altitude from a value of 1.13×10^{-4} W kg^{-1} at 5 km up to 2.50×10^{-4} W kg^{-1} at 16 km with a slight inversion just below the tropopause (about 10 km). Our statistical

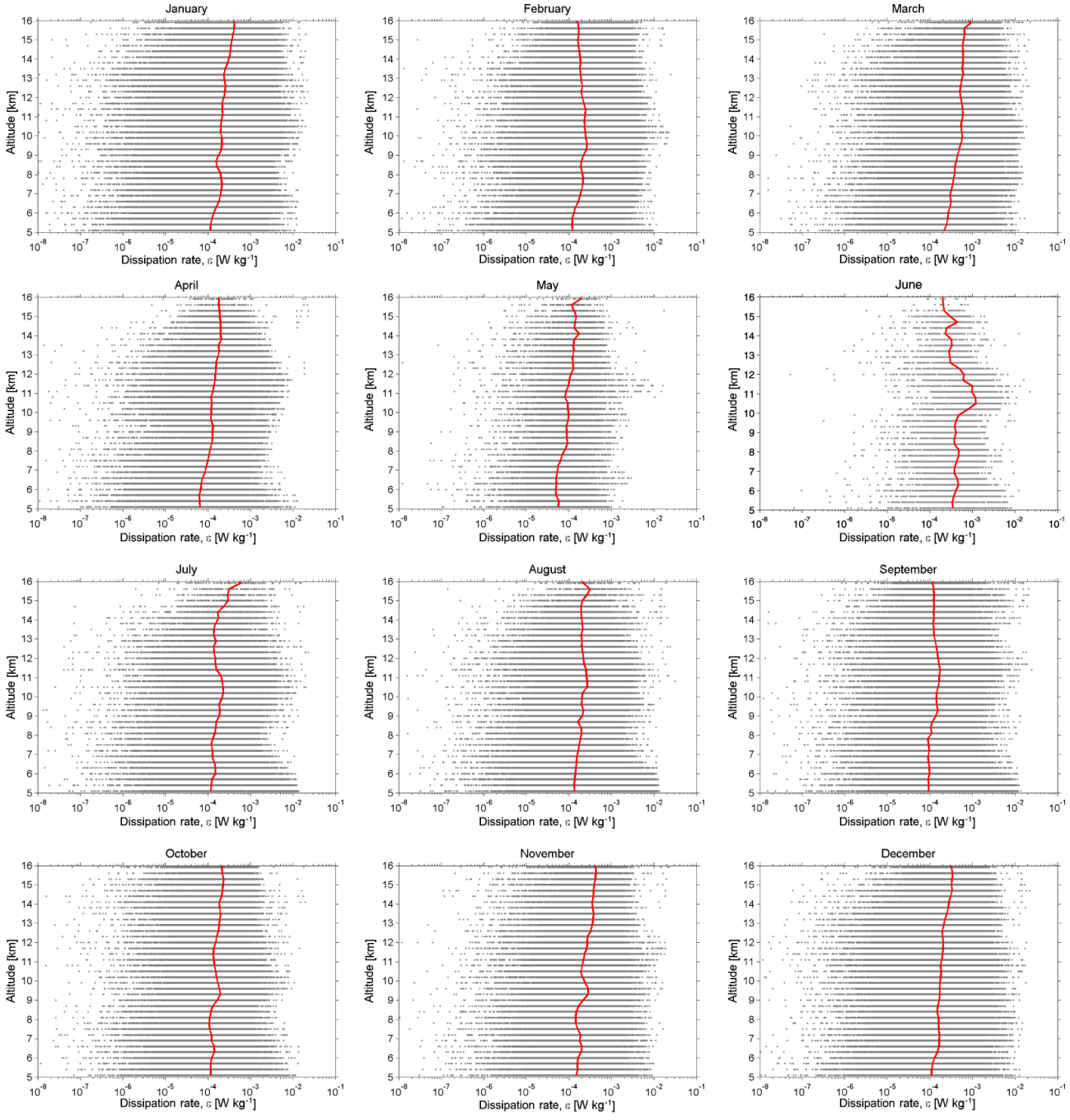

Figure 9. Scatter plots of turbulent energy dissipation rate derived from the radar observations with MAARSY in the years of 2011–2013 for different months and the corresponding median values shown in red (solid lines).

results of ε derived from radar measurements are consistent with the values obtained in previous studies (e.g. Nastrom and Eaton, 1997; Satheesan and Murthy, 2004; Kantha and Hocking, 2011), though, the ε values shown in the current study are derived based on a much larger data set. The increase in ε with altitude has also been described by Haack et al. (2014), who used the balloon-borne instrument LITOS to measure ε in the altitude range from 7 up to 29 km. Note that their results are achieved based on two individual flights at Kiruna (67° N, 21° E). We note that different findings on the height dependence of ε have also been described by, for example, Clayson and Kantha (2008), who obtained larger dissipation rates in the troposphere than in the lower stratosphere.

Further, we show scatter plots of ε as a function of altitude and their median values in each month in Fig. 9.

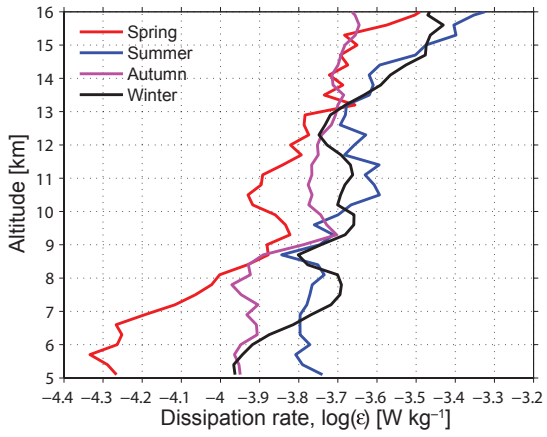

Figure 10. Vertical profiles of the seasonal medians of ε observed from the radar observations with MAARSY during different seasons in the years of 2010–2013: spring (March–May), summer (June–August), autumn (September–November), and winter (December–February).

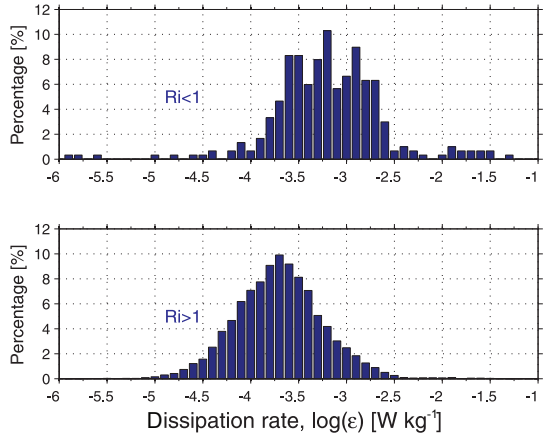

Figure 11. Histograms of energy dissipation rates ε derived from the radar measurements with MAARSY in the years of 2010–2013 under the conditions of $Ri < 1$ (upper panel) and $Ri > 1$ (lower panel), respectively.

Most of the ε values fall within the range between 10^{-7} and $10^{-2}\,\mathrm{W\,kg^{-1}}$, covering 5 orders of magnitude. The widths of ε distributions are larger in the troposphere than in the lower stratosphere. Generally, the vertical profiles of the ε median consistently show an increase in energy dissipation rates from the upper troposphere to the lower stratosphere with fluctuations near the tropopause, except for the month of June (but note that there are only 4 days of observation in June).

In order to illustrate the seasonal variation of the energy dissipation rates, we show the vertical profiles of the ε median in different seasons (spring: March–May; summer: June–August; autumn: September–November; and winter: December–February) in Fig. 10. All four profiles show

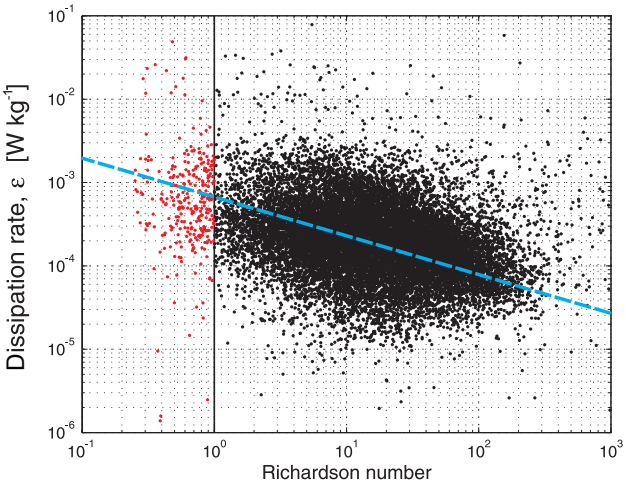

Figure 12. Scatter plot of energy dissipation rates ε derived from the radar measurements with MAARSY vs. the Richardson number in logarithmic scales in the years of 2010–2013. Both data sets are analysed with a height resolution of 300 m. All values at the condition of $Ri < 1$ ($Ri > 1$) are marked in red (black). The $Ri = 1$ line is indicated in black. The dashed line indicates an expected linear anti-correlation between the two quantities shown.

a height dependence of ε in that the energy dissipate rates generally increase with altitudes, which has been presented above. The ε medians in summer and winter are very close, especially in the lower stratosphere, and larger compared with the values at the equinoxes by a factor of 1.5–2.0. In addition, atmospheric turbulence derived from our radar measurements reveals no diurnal variation in the UTLS regions (at altitudes of 5 km and above), i.e. remaining nearly constant over the whole day especially in the stratosphere (not shown here). This is different from the case in the atmospheric boundary layer (within the altitudes of a few hundred metres) where turbulence has a prominent diurnal variation reaching a maximum around midday (e.g. Yasuda, 1988; Englberger and Dörnbrack, 2016).

5 Discussion

Due to the importance of turbulence in atmospheric dynamics, a wealth of theoretical and experimental efforts has been carried out to identify the generation mechanisms, which are not fully quantified or understood (Wyngaard, 1992; Lübken, 1992, 1997; Fritts et al., 2003; Müllemann et al., 2003; Rapp et al., 2004; Sharman et al., 2012; Schneider et al., 2015; Fritts et al., 2016, e.g.). According to the theory described above, turbulence is under the influence of shear and buoyancy forces, but not only of those. Because of the lack of temperature measurements, we are not able to determine the buoyancy contribution to turbulence. Simultaneous measurements involving temperature with, e.g., lidar are highly desir-

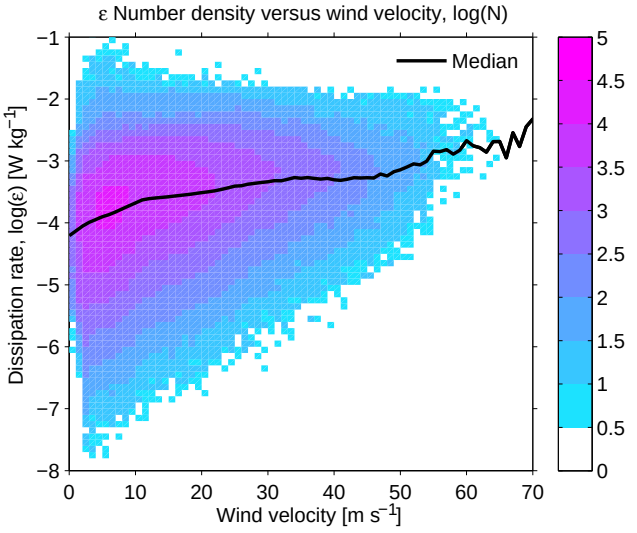

Figure 13. Number density of the derived turbulent energy dissipation rate ε vs. wind velocity (horizontal) derived from the radar measurements with MAARSY in the years of 2010–2013. The condition with stronger winds tends to lead to the occurrence of stronger turbulence, whereas weaker turbulence only occurred where there was weaker wind. The ε median for every 1 m s^{-1} interval of wind velocity shown in black reveals an increase with the increased wind velocities.

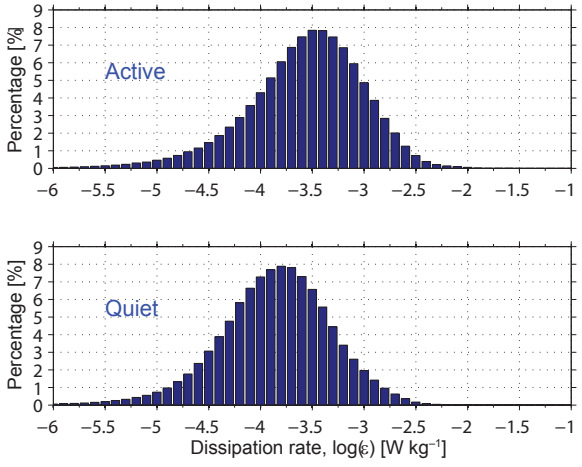

Figure 14. Histograms of the derived turbulent energy dissipation rates ε from the radar measurements with MAARSY in the years of 2010–2013 under active (upper panel) and quiet (lower panel) conditions. The ε values for both cases reveal a log-normal distribution as stated above.

able for further study in the future. In this section, we compare the derived ε with the background conditions, i.e. the Richardson number, the velocity of horizontal wind, and the vertical shear of horizontal wind.

As mentioned above, a classical approach to analysing the relation between turbulence and the atmospheric background condition is to determine the Richardson number Ri. Here we determine the vertical shear of horizontal wind velocities from radar observations and the Brunt–Väisälä frequency N from the ECMWF reanalysis data with a height resolution of 300 m. These values are used to calculate $Ri = N^2/\left(\frac{\mathrm{d}\overline{U}}{\mathrm{d}z}\right)^2$. The derived ε values are split into two groups for the conditions of $Ri < 1$ and $Ri > 1$. Figure 11 shows the normalized histograms of the derived ε in percentage under the conditions of $Ri < 1$ (upper panel) and $Ri > 1$ (lower panel), respectively. For both cases, the ε values are highly variable ranging from 1.44×10^{-4} to 2.76×10^{-3} W kg^{-1} under the condition of $Ri < 1$ and from 2.82×10^{-5} to 8.91×10^{-4} W kg^{-1} under $Ri > 1$ (only considering the values with the histograms larger than 2 %); i.e., the statistical results show that the ε values under the condition of $Ri < 1$ are much larger than under $Ri > 1$. In Fig. 12 we show a scatter plot of ε vs. Ri with the data points in red under the condition of $Ri < 1$ and in black under $Ri > 1$. The relation between ε and Ri has been shown in the literature to depend on the scale (i.e. height resolution) over which Ri has been calculated. The N^2 values derived from the ECMWF reanalysis data are positive in general, and hence $Ri > 0$ here. During the period to determine ε in this study, the Ri values estimated from the ECMWF reanalysis data are highly variable, ranging from 0.1 up to 1000. Figure 12 shows that the large majority of turbulent eddies exist under the condition of $Ri > 1$ (black points), which, however, indicates stability. These findings are consistent with the results by Haack et al. (2014), who calculated Ri over the scales of 10, 70, and 200 m. There are much fewer data for ε under the condition of $Ri < 1$ (red points; only 1.7 % in total), which, however, reveal much larger values. The histograms of ε (not shown here) show that the median (mean) values of ε are 5.18×10^{-4} W kg^{-1} (1.02×10^{-3} W kg^{-1}) under the condition of $Ri < 1$ and 1.61×10^{-4} W kg^{-1} (3.24×10^{-4} W kg^{-1}) under $Ri > 1$. In addition, the scatter plot of all values shows that there is a roughly negative correlation between ε and Ri that is independent of the scale dependence of Ri (see the dashed line).

Wind field also plays a role in the generation of turbulence (indirectly), since there is a strong interaction between gravity waves (GWs) and the background wind field (Sato, 1994; Fritts et al., 2003; Rapp et al., 2004). Figure 13 shows the number density of the turbulent energy dissipation rates (in logarithmic values) against the corresponding background wind velocities derived from the radar measurements with MAARSY. The number density shows peaks with wind velocity within 4–9 m s^{-1} and ε within 7.94×10^{-5}–3.98×10^{-4} W kg^{-1}. The range of the ε values becomes narrower as the wind velocities become stronger. It seems that the condition with stronger winds only tends to appear with the occurrence of stronger turbulence (e.g. $\varepsilon > 10^{-4}$ W kg^{-1}). The ε distribution against the background wind fields statistically

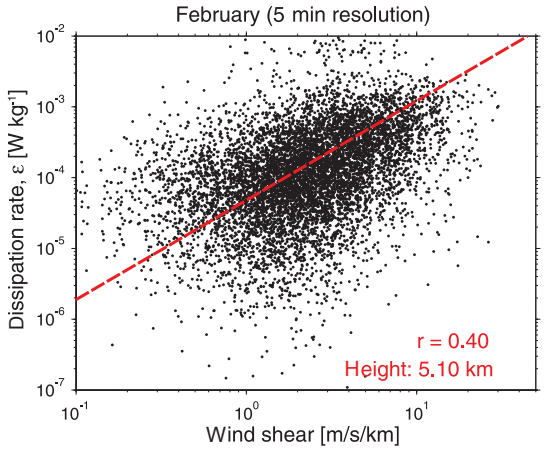

Figure 15. Scatter plot of the turbulent energy dissipation rates ε vs. the vertical shears of horizontal wind derived from the radar measurements with MAARSY in logarithmic scales. The values were derived based on all the data with 5 min resolution in February in the years 2010–2013 at an altitude of 5.1 km. The dashed line indicates an expected linear correlation between the two shown quantities. The corresponding correlation coefficient r is indicated in the lower right corner, which is highly significant, i.e. well above the 99.9 % level.

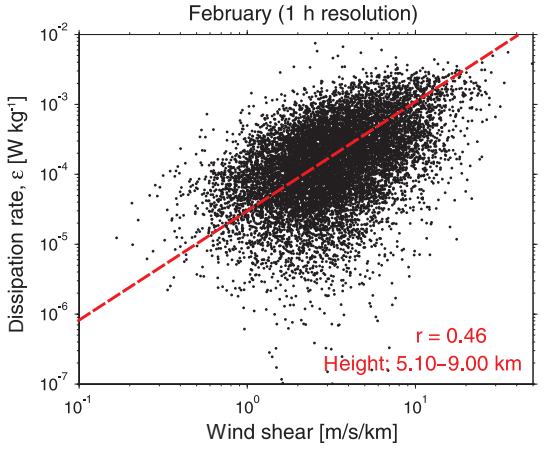

Figure 16. Same as Fig. 15, but for the results derived based on all the data with 1 h resolution in February in the years 2010–2013 at altitudes of 5.1–9.0 km. The corresponding correlation coefficient r is indicated in the lower right corner, which is highly significant, i.e. well above the 99.9 % level.

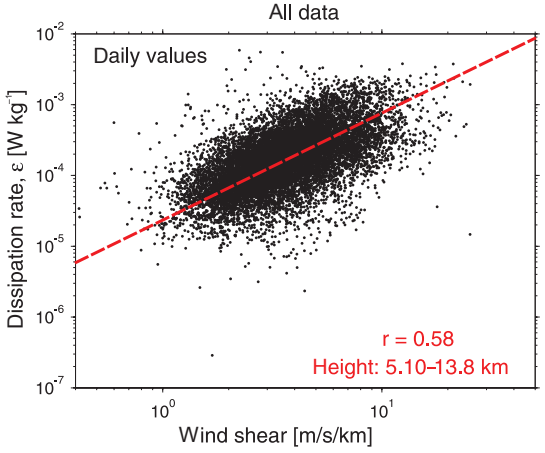

Figure 17. Same as Fig. 15, but for the results derived based on all the data with 1-day resolution in the years 2010–2013 at altitudes of 5.1–13.8 km. The corresponding correlation coefficient r is indicated in the lower right corner, which is highly significant, i.e. well above the 99.9 % level.

shows that the upper edge of turbulence (maxima) occurred independently of winds, whereas the lower edge (minima) reveals a positive correlation with winds. In addition, the minima of ε gradually decay with the decrease in wind velocities indicating that there was no instrumental bias included. The black solid line shows the ε median inferred for every $1\,\mathrm{m\,s^{-1}}$ interval of wind velocity, which generally reveals an increase with the increased wind velocities. Further, there are steeper increases during the wind velocities falling within the range of 0–11 and of $> 48\,\mathrm{m\,s^{-1}}$. Following the wind criterion by Ecklund et al. (1986), the quiet dynamic condition is defined as the condition with background wind velocities less than $10\,\mathrm{m\,s^{-1}}$ and active dynamic conditions with velocities larger than $10\,\mathrm{m\,s^{-1}}$. The derived dissipation rates ε are split into two data sets for active and quiet conditions. In Fig. 14 we show the normalized ε histograms in percentage under active (upper panel) and quiet (lower panel) conditions. For both cases, the ε distributions look like they are log-normal with a negative skewness and the large majority of ε falls within the range between 10^{-6} and $10^{-2}\,\mathrm{W\,kg^{-1}}$ (99.73 % for active conditions and 99.72 % for quiet conditions). However, the comparison reveals that dissipation rates are larger under active conditions with the data sets peaking at $3.16 \times 10^{-4}\,\mathrm{W\,kg^{-1}}$ than under quiet conditions peaking at $1.58 \times 10^{-4}\,\mathrm{W\,kg^{-1}}$.

According to Eq. (A5) in the Appendix, we arrive at the following relation:

$$\varepsilon = K_\mathrm{m} \cdot \left(\frac{\mathrm{d}\overline{U}}{\mathrm{d}z}\right)^2 = -\overline{U'w'} \cdot \left(\frac{\mathrm{d}\overline{U}}{\mathrm{d}z}\right), \tag{10}$$

where the term $\overline{U'w'}$ is the vertical flux of horizontal momentum. Thus, shear production is the net conversion rate per unit mass from the kinetic energy of the mean flow into turbulence. The momentum flux with a component opposite the mean wind shear leads to a positive shear production. With the assumption that the total flux of momentum with height

is constant for a limited period, we can expect a linear correlation between dissipation rate and wind shear. In Fig. 15, we present a scatter plot of the derived ε vs. the corresponding wind shears derived from the radar measurements (5 min resolution) in February at an altitude of 5.1 km. The dashed line indicates an expected linear correlation with a correlation coefficient $r = 0.4$ between the two quantities shown. In addition, Fig. 16 shows the same as Fig. 15, but for the results derived from the radar measurements with 1 h resolution in February at altitudes of 5.1–9.0 km. Finally, we carry out the same exercise for all the data available for this study on a daily-value basis (i.e. 1-day resolution) and infer the statistical results of the correlation shown in Fig. 17. They again reveal a linear correlation between ε and the wind shears with a corresponding correlation coefficient of 58 %, well above the 99.9 % level. In summary, the three cases with different temporal resolutions reveal that there is a linear correlation between the turbulent energy dissipation rates and the wind shears which is highly significant. Hence the wind shears play an important role (through the Kelvin–Helmholtz instability; e.g. Fritts et al., 2003, 2012) in the generation and/or maintenance of turbulence.

6 Conclusions

In the current paper we have presented the derivation of the turbulent energy dissipation rate ε from radar measurements with MAARSY based on the conversion of spectral widths as well as from in situ measurements with balloon-borne radiosondes at the radar site of MAARSY applying Thorpe analysis. Before converting spectral widths to ε we carefully removed the broadening effects due to the finite beam width of MAARSY. The corrected spectral widths are much smaller than the observed ones, indicating that horizontal winds have a dominating influence on the observed spectral widths. The estimate of the constant C_K is key for applying Thorpe analysis. Here we use $C_K = 1$, which is only valid for the case when turbulence is well developed. We then compared the simultaneous measurements of ε from both techniques with $C_K = 1$ when applying Thorpe analysis. An encouraging agreement was found in terms of the ε values derived with both instruments falling within a similar range and with their histogram peaking at about the same value. The comparison should be considered as a way to validate the derivation of the turbulence parameter from radar measurements based on the collocated in situ measurements with balloon-borne radiosondes. Conversely, it also provides a method to calibrate the value of C_K, which is a key parameter used in Thorpe analysis. As a caveat it needs to be mentioned that recent direct numerical simulations by Fritts et al. (2016) question the validity of using a constant value of c (hence C_K). Nevertheless, it is remarkable how well radiosonde and radar data in this study show agreement with each other using just this approach.

From a total of 522 days of observations with MAARSY during the period of 2010–2013, we derived a preliminary climatology of turbulence in the free atmosphere. The derived ε shows variability of about 5 orders of magnitude inherent in the dissipation rates falling within the range between 10^{-7} and $10^{-2}\,\mathrm{W\,kg^{-1}}$. The ε distribution is approximately log-normal, as expected for an intermittent process like turbulence. The ε profiles show an increase with altitude with the medians from a value of 1.13×10^{-4} up to $2.50 \times 10^{-4}\,\mathrm{W\,kg^{-1}}$. This height dependence is also derived from the data in each individual month. Furthermore, the coverage of the ε distribution is wider in the troposphere than in the lower stratosphere. Atmospheric turbulence based on our radar measurements reveals a seasonal variation in that the ε medians are larger during summer and winter than during the equinoxes by nearly a factor of 2. No clear diurnal variation is found in ε with MAARSY, which remains nearly constant over the whole day in the UTLS regions (from 5 km upwards in the current study).

With the derivation of wind shear from radar and the Brunt–Väisälä frequency N from the ECMWF reanalysis data, we calculated the Richardson number Ri with which the dissipation rates are compared. The statistical results from our data show that the majority of turbulent eddies exist under the conditions of $Ri > 1$ (more than 98 % of all the data). The ε values are significantly larger under the condition of $Ri < 1$ than under $Ri > 1$. The median (mean) values of the ε derived from MAARSY are $5.18 \times 10^{-4}\,\mathrm{W\,kg^{-1}}$ ($1.02 \times 10^{-3}\,\mathrm{W\,kg^{-1}}$) under $Ri < 1$ and $1.61 \times 10^{-4}\,\mathrm{W\,kg^{-1}}$ ($3.24 \times 10^{-4}\,\mathrm{W\,kg^{-1}}$) under $Ri > 1$. In addition, the scatter plot of the derived ε vs. Ri reveals a roughly negative correlation between the two quantities that is independent of the scale dependence of Ri. Similar properties are also found from individual profiles with radiosondes; i.e. stronger turbulence occurs where Ri is relatively smaller and vice versa. However, no clear threshold value of $Ri_c = 1/4$ is recognized in our data.

In order to study the influence of background wind fields on turbulence, we presented the number densities of ε vs. the background wind fields, showing that the ranges of the ε values become narrower as the winds become stronger and the condition with stronger winds only tends to appear with the occurrence of strong turbulence. The derived ε were further split into two groups for active and quiet conditions. The dissipation rates under active conditions are much larger than under quiet conditions, indicating that stronger winds (e.g. $U > 10\,\mathrm{m\,s^{-1}}$) appear to create more turbulent eddies.

Last but not least, we compared the derived ε with the corresponding vertical shears of horizontal wind according to the relation that the turbulent energy dissipation rate may be expressed as the production of momentum flux and wind shear. We then inferred the comparison between the derived ε and the corresponding wind shears based on the radar measurements with different temporal resolutions, i.e. 5 min, 1 h, and 1 day. The three cases all reveal a nearly linear cor-

relation between the turbulent energy dissipation rates and the corresponding wind shears, which is highly significant. Kelvin–Helmholtz instabilities occurring under conditions of wind shear are well known to cause turbulence (e.g. Fritts et al., 2003, 2012). The statistical results reveal that the turbulent energy dissipation rate does indeed follow the dependence of the corresponding wind shears. Our findings hence provide support for the idea that wind shears play an important role in the generation of turbulence in the troposphere and lower stratosphere.

7 Data availability

The data sets with the MAARSY radar used in this study are stored in the Leibniz-Institut für Atmosphärenphysik (IAP) repository and are available upon request (contact email: chau@iap-kborn.de). The radiosonde data sets can be requested by contacting the first author of this paper.

Appendix A: The dynamics of turbulence

In homogeneous (isotropic) turbulence, the turbulence intensity is usually represented as the turbulent kinetic energy per unit mass (E_k), which is given by the root-mean-square velocity fluctuations, i.e.

$$E_\mathrm{k} = \frac{1}{2}\left(\overline{u'^2} + \overline{v'^2} + \overline{w'^2}\right), \tag{A1}$$

where u', v', and w' are the fluctuating parts of zonal, meridional, and vertical winds, respectively. E_k is a pure function of time and satisfies the budget

$$\frac{\mathrm{d}E_\mathrm{k}}{\mathrm{d}t} = P - B - \varepsilon, \tag{A2}$$

where P is the shear production and B the buoyancy destruction. The expressions for them read

$$P = -\overline{U'w'}\frac{\mathrm{d}\overline{U}}{\mathrm{d}z} = K_\mathrm{m}\left(\frac{\mathrm{d}\overline{U}}{\mathrm{d}z}\right)^2, \tag{A3}$$

where $U = \sqrt{u^2 + v^2}$ is the velocity of horizontal wind, $K_\mathrm{m} = -\overline{U'w'}/(\mathrm{d}\overline{U}/\mathrm{d}z)$ the turbulent diffusion coefficient for momentum, and $\mathrm{d}\overline{U}/\mathrm{d}z$ the wind shear, and

$$B = -\frac{g}{\overline{\theta}}\overline{w'\theta'} = K_h N^2, \tag{A4}$$

where θ is the generalized potential temperature, $\overline{\theta}$ a reference state, $K_h = -\overline{U'\theta'}/(\mathrm{d}\overline{\theta}/\mathrm{d}z)$ the turbulent diffusion coefficient for heat, and $N = \sqrt{g/\theta \cdot \mathrm{d}\theta/\mathrm{d}z}$ the Brunt–Väisälä frequency. With the derivation of ε, K_m can be inferred based on the following relationship (Tatarskii, 1971):

$$K_\mathrm{m} = \varepsilon \Big/ \left(\frac{\mathrm{d}\overline{U}}{\mathrm{d}z}\right)^2. \tag{A5}$$

And K_h can be inferred based on the following relationship (Lilly et al., 1974):

$$K_h = \gamma\frac{\varepsilon}{N^2}, \tag{A6}$$

where γ is referred to as the mixing efficiency. Under the hypotheses of homogeneity and stationarity, $\gamma = B/(P - B)$. Using $B/P = 0.2$, a value that is mostly used in the literature, gives $\gamma = 0.25$.

For stationary turbulence, i.e. $\mathrm{d}E_\mathrm{k}/\mathrm{d}z = 0$, the energy dissipation rate ε can be written

$$\varepsilon = P - B. \tag{A7}$$

Hence, the turbulence development, whether it grows or decays, depends on the relative magnitude of the shear and buoyancy contributions. The ratio between the two terms is defined as a flux Richardson number, a parameter for monitoring the turbulence activity in the medium:

$$Ri_\mathrm{f} = \frac{B}{P} = \frac{K_h}{K_\mathrm{m}}Ri = \frac{1}{Pr}Ri, \tag{A8}$$

where $Ri = N^2/\left(\frac{\mathrm{d}\overline{U}}{\mathrm{d}z}\right)^2$ is the gradient Richardson number and $Pr = K_\mathrm{m}/K_h$ the turbulent Prandtl number. Pr describes the ratio of turbulent flux momentum to the turbulent heat conduction and is not a constant near unity but varies highly within a range between 1 and 10 (e.g. Justus, 1967; Fritts and Dunkerton, 1985).

Acknowledgements. The authors would like to thank J. L. Chau for support in MAARSY data handling. Q. Li and M. Rapp acknowledge support by the German Ministry for Education and Research (BMBF) in the scope of the ROMIC-GWLCYCLE Project. Support for A. Schön and G. Stober was provided by the BMBF ROMIC-METROSI Project and for A. Schneider by the International Leibniz Graduate School for Gravity Waves and Turbulence in the Atmosphere and Ocean (ILWAO) funded by the Leibniz Association (WGL).

The article processing charges for this open-access publication were covered by a Research Centre of the Helmholtz Association.

The topical editor, V. Kotroni, thanks two anonymous referees for help in evaluating this paper.

References

Achatz, U.: Gravity-wave breaking: Linear and primary nonlinear dynamics, Adv. Space Sci., 40, 719–733, 2007.

Balsley, B. B., Svensson, G., and Tjernström, M.: On the scale-dependence of the gradient Richardson number in the residual layer, Bound. Lay.-Meteorol., 127, 57–72, 2008.

Bertin, F., Campistron, B., Caccia, J. L., and Wilson, R.: Mixing processes in a tropopause folding observed by a network of ST radar and lidar, Ann. Geophys., 19, 953–963, doi:10.5194/angeo-19-953-2001, 2001.

Birner, T.: Fine-scale structure of the extratropical tropopause region, J. Geophys. Res., 111, D04104, doi:10.1029/2005JD006301, 2006.

Chau, J. L. and Kudeki, E.: First E- and D-region incoherent scatter spectra observed over Jicamarca, Ann. Geophys., 24, 1295–1303, doi:10.5194/angeo-24-1295-2006, 2006.

Chau, J. L., Strelnikova, I., Schult, C., Oppenheim, M. M., Kelley, M. C., Stober, G., and Singer, W.: Nonspecular meteor trails from non-field-aligned irregularities: Can they be explained by presence of charged meteor dust?, Geophys. Res. Lett., 41, 3336–3343, doi:10.1002/2014GL059922, 2014.

Clayson, C. A. and Kantha, L.: On turbulence and mixing in the free atmosphere inferred from high-resolution soundings, J. Atmos. Ocean. Tech., 25, 833–852, 2008.

Dehghan, A. and Hocking, W. K.: Instrumental errors in spectral-width turbulence measurements by radars, J. Atmos. Sol.-Terr. Phy., 73, 1052–1068, 2011.

Dillon, T. M.: Vertical overturns: A comparison of Thorpe and Ozmidov length scales, J. Geophys. Res., 87, 9601–9613, 1982.

Ecklund, W. L., Gage, K. S., Nastrom, G. D., and Balsley, B. B.: A preliminary climatology of the spectrum of vertical velocity observed by clear-air Doppler radar, J. Clim. Appl. Meteorol., 25, 885–892, 1986.

Englberger, A. and Dörnbrack, A.: The impact of the diurnal cycle of the atmospheric boundary layer on physical variables relevant for wind energy applications, Atmos. Chem. Phys. Discuss., doi:10.5194/acp-2015-995, in review, 2016.

Engler, N., Latteck, R., Strelnikov, B., Singer, W., and Rapp, M.: Turbulent energy dissipation rates observed by Doppler MST Radar and by rocket-borne instruments during the MIDAS/MaCWAVE campaign 2002, Ann. Geophys., 23, 1147–1156, doi:10.5194/angeo-23-1147-2005, 2005.

Frehlich, R., Meilleier, Y., Jensen, M. L., and Balsley, B.: A statistical description of small-scale turbulence in the low-level nocturnal jet, J. Atmos. Sci., 61, 1079–1085, 2004.

Fritts, D. C. and Alexander, M. J.: Gravity wave dynamics and effects in the middle atmosphere, Rev. Geophys., 41, 1003, doi:10.1029/2001RG000106, 2003.

Fritts, D. C. and Dunkerton, T. J.: Fluxes of heat and constituents due to convectively unstable gravity waves, J. Atmos. Sci., 42, 549–556, 1985.

Fritts, D. C., Bizon, C., Werne, J. A., and Meyer, C. K.: Layering accompanying turbulence generation due to shear instability and gravity-wave breaking, J. Geophys. Res., 108, 8452, doi:10.1029/2002JD002406, 2003.

Fritts, D. C., Wan, K., Franke, P. M., and Lund, T.: Computation of clear-air radar backscatter from numerical simulations of turbulence: 3. Off-zenith measurements and biases throughout the lifecycle of a Kelvin-Helmholtz instability, J. Geophys. Res., 117, D17101, doi:10.1029/2011JD017179, 2012.

Fritts, D. C., Wang, L., Geller, M. A., Lawrence, D. A., Werne, J., and Balsley, B. B.: Numerical modeling of multiscale dynamics at a high Reynolds number: Instabilities, turbulence, and an assessment of Ozmidov and Thorpe scales, J. Atmos. Sci., 73, 555–578, 2016.

Gage, K. S. and Balsley, B. B.: On the scattering and reflection mechanisms contributing to clear air radar echoes from the troposphere, stratosphere, mesosphere, Radio Sci., 15, 243–257, 1980.

Gage, K. S. and Green, J. L.: An objective method for the determination of tropopause height from VHF radar observaions, J. Appl. Meteorol., 21, 1150–1154, 1982.

Gage, K. S., Balsley, B. B., and Green, J. L.: Fresnel scattering model for the specular echoes observed by VHF radar, Radio Sci., 16, 1447–1453, 1981.

Gage, K. S., Ecklund, W. L., and Balsley, B. B.: A modified Fresnel scattering model for the parameterization of Fresnel returns, Radio Sci., 20, 1493–1501, 1985.

Gavrilov, N. M., Luce, H., Crochet, M., Dalaudier, F., and Fukao, S.: Turbulence parameter estimations from high-resolution balloon temperature measurements of the MUTSI-2000 campaign, Ann. Geophys., 23, 2401–2413, doi:10.5194/angeo-23-2401-2005, 2005.

Haack, A., Gerding, M., and Lübken, F.-J.: Characteristics of stratospheric turbulent layers measured by LITOS and their relation to the Richardson number, J. Geophys. Res.-Atmos., 119, 10605–10618, doi:10.1002/2013JD021008, 2014.

Hall, C. M., Röttger, J., Kuyeng, K., Sigernes, F., Claes, S., and Chau, J.: First results of the refurbished SOUSY radar: Tropopause altitude climatology at 78° N, 16° E, 2008, Radio Sci., 44, RS5008, doi:10.1029/2009RS004144, 2009.

Hocking, W. K.: On the extraction of atmospheric turbulence parameters from radar backscatter Doppler spectra-I. Theory, J. Atmos. Terr. Phys., 45, 89–102, 1983.

Hocking, W. K.: Measurements of turbulent energy dissipation rates in the middle atmosphere by radar techniques: A review, Radio Sci., 20, 1403–1422, 1985.

Justus, C. G.: The eddy diffusivities, energy balance parameters, and heating rate of upper atmospheric turbulence, J. Geophys. Res., 72, 1035–1039, 1967.

Kantha, L. and Hocking, W.: Dissipation rates of turbulence kinetic energy in the free atmosphere: MST radar and radiosondes, J. Atmos. Sol.-Terr. Phy., 73, 1043–1051, doi:10.1016/j.jastp.2010.11.024, 2011.

Klostermeyer, J. and Rüster, R.: Radar observation and model computation of a jet stream-generated Kelvin-Helmholtz instability, J. Geophys. Res., 85, 2841–2846, 1980.

Kudeki, E., Bhattacharyya, S., and Woodman, R. F.: A new approach in incoherent scatter F region $E \times B$ drift measurements at Jicamarca, J. Geophys. Res., 104, 28145–28162, doi:10.1029/1998JA900110, 1999.

Lane, T. P. and Sharman, R. D.: Intensity of thunderstorm-generated turbulence revealed by large-eddy simulation, Geophys. Res. Lett., 41, 2221–2227, doi:10.1002/2014GL059299, 2014.

Larsen, M. F. and Röttger, J.: Comparison of tropopause height and frontal boundary locations based on radar radiosonde data, Geophys. Res. Lett., 10, 325–328, 1983.

Latteck, R. and Strelnikova, I.: Extended observations of polar mesospheric winter echoes over Andøya (69° N) using MAARSY, J. Geophys. Res., 120, 8216–8226, doi:10.1002/2015JD023291, 2015.

Latteck, R., Singer, W., Rapp, M., and Renkwitz, T.: MAARSY-the new MST radar on Andøya/Norway, Adv. Radio Sci., 8, 219–224, doi:10.5194/ars-8-219-2010, 2010.

Latteck, R., Singer, W., Rapp, M., Vandepeer, B., Renkwitz, T., Zecha, M., and Stober, G.: MAARSY: The new MST radar on Andøya – System description and first results, Radio Sci., 47, RS1006, doi:10.1029/2011RS004775, 2012.

Lilly, D. K., Waco, D. E., and Adelfang, S. I.: Stratospheric mixing estimated from high-altitude turbulence measurements, J. Appl. Meteorol., 13, 488–493, 1974.

Lindzen, R. S.: Turbulence and stress owing to gravity wave and tidal breakdown, J. Geophys. Res., 86, 9707–9714, doi:10.1029/JC086iC10p09707, 1981.

Luce, H., Fukao, S., Dalaudier, F., and Crochet, M.: Strong Mixing Events Observed near the Tropopause with the MU Radar and High-Resolution Balloon Techniques, J. Atmos. Sci., 59, 2885–2896, 2002.

Lübken, F.-J., von Zahn, U., Thrane, E. V., Blix, T. A., Kokin, G. A., and Pachomov, S. V.: In situ measurements of turbulence energy dissipation rates and eddy diffusion coefficients during MAP/WINE, J. Atmos. Terr. Phys., 49, 763–775, 1987.

Lübken, F.-J.: On the extraction of turbulent parameters from atmospheric density fluctuations, J. Geophys. Res., 97, 20385–20395, 1992.

Lübken, F.-J.: Seasonal variation of turbulent energy dissipation rates at high latitudes as determined by in situ measurements of neutral density fluctuations, J. Geophys. Res., 102, 13441–13456, 1997.

Mihalikova, M., Kirkwood, S., Arnault, J., and Mikhaylova, D.: Observation of a tropopause fold by MARA VHF wind-profiler radar and ozonesonde at Wasa, Antarctica: comparison with ECMWF analysis and a WRF model simulation, Ann. Geophys., 30, 1411–1421, doi:10.5194/angeo-30-1411-2012, 2012.

Mater, B. D., Schaad, S. M., and Venayagamoorthy, S. K.: Relevance of the Thorpe length scale in stably stratified turbulence, Phys. Fluids, 25, 076604, doi:10.1063/1.4813809, 2013.

Mega, T., Yamamoto, M. K., Luce, H., Tabata, Y., Hashiguchi, H., Yamamoto, M. M. D., Yamanaka, M., and Fukao, S.: Turbulence generation by Kelvin-Helmholtz instability in the tropical tropopause layer observed with a 47 MHz range imaging radar, J. Geophys. Res., 115, D18115, doi:10.1029/2010JD013864, 2010.

Miles, J. W.: On the stability of heteorgeneous shear flow, J. Fluid Mech., 10, 496–508, 1961.

Müllemann, A., Rapp, M., Lübken, F.-J.: Morphology of turbulence in the polar summer mesopause region during the MIDAS/SOLSTICE campaign 2001, Adv. Space Res., 31, 2069–2074, 2003.

Murphy, D. J., Hocking, W. K., and Fritts, D. C.: An assessment of the effect of gravity waves on the width of radar Doppler spectra, J. Atmos. Terr. Phys., 56, 17–29, 1994.

Nastrom, G. D. and Eaton, F. D.: Turbulence eddy dissipation rates from radar observations at 5–20 km at white sands missile range, New Mexico, J. Geophys. Res., 102, 19495–19505, 1997.

Nastrom, G. D. and Gage, K. S.: A climatology at atmospheric wavenumber spectra of wind and temperature observed by commercial aircraft, J. Atmos. Sci., 42, 950–960, 1985.

O'Connor, E. J., Illingworth, A. J., Brooks, I. M., Westbrook, C. D., Hogan, R. J., Davies, F., and Brooks, B. J.: A method for estimating the turbulent kinetic energy dissipation rate from a vertically pointing Doppler lidar, and independent evaluation from balloon-borne in situ measurements, J. Atmos. Ocean. Tech., 27, 1652–1664, 2010.

Ottersten, H.: Mean vertical gradient of potential refractive index in turbulent mixing and radar detection of CAT, Radio Sci., 4, 1247–1249, 1969.

Pantley, K. C. and Lester, P. F.: Observations of severe turbulence near thunderstorm tops, J. Appl. Meteorol., 29, 1171–1179, 1990.

Pavelin, E. G. and Whiteway, J.: Gravity wave interactions around the jet stream, Geophys. Res. Lett., 29, 2024, doi:10.1029/2002GL015783, 2002.

Rapp, M., Strelnikov, B., Müllemann, A., and Lübken, F.-J.: Turbulence measurements and implications for gravity wave dissipation during the MaCWAVE/MIDAS rocket program, Geophys. Res. Lett., 31, L24S07, doi:10.1029/2003GL019325, 2004.

Rapp, M., Strelnikova, I., Latteck, R., Hoffmann, P., Hoppe, U.-P., Häggström, I., and Rietveld, M. T.: Polar mesosphere summer echoes (PMSE) studied at Bragg wavelengths of 2.8 m, 67 cm, and 16 cm, J. Atmos. Sol.-Terr. Phy., 70, 947–961, 2008.

Rapp, M., Latteck, R., Stober, G., Hoffmann, P., Singer, W., and Zecha, M.: First three-dimentional observations of polar mesosphere winter echoes: Resolving space-time ambiguity, J. Geophys. Res., 116, A11307, doi:10.1029/2011JA016858, 2011.

Renkwitz, T., Singer, W., Latteck, R., Stober, G., and Rapp, M.: Validation of the radiation pattern of the Middle Atmosphere Alomar Radar System (MAARSY), Adv. Radio Sci., 10, 245–253, doi:10.5194/ars-10-245-2012, 2012.

Renkwitz, T., Stober, G., Latteck, R., Singer, W., and Rapp, M.: New experiments to validate the radiation pattern of the Middle Atmosphere Alomar Radar System (MAARSY), Adv. Radio Sci., 11, 283–289, doi:10.5194/ars-11-283-2013, 2013.

Röttger, J.: VHF radar observations of a frontal passage, J. Appl. Meteorol., 18, 85–91, 1979.

Röttger, J. and Larsen, M. F.: UHF/VHF radar techniques for atmospheric research and wind profiler applications, Radar in Meteorology, D. Atlas, Ed., Amer. Meteor. Soc., 806 pp., 1990.

Satheesan, K. and Murthy, B. V. K.: Estimation of turbulence parameters in the lower atmosphere from MST radar observations, Q. J. Roy. Meteor. Soc., 130, 1235–1249, doi:10.1256/qj.03.86, 2004.

Sato, K.: A statistical study of the structure, saturation and sources of inertia-gravity waves in the lower stratosphere observed with the MU radar, J. Atmos. Terr. Phys., 56, 755–774, 1994.

Sharman, R. D., Doyle, J. D., and Shapiro, M. A.: An investigation of a commercial aircraft encounter with severe clear-air turbulence over western Greenland, J. Appl. Meteorol. Clim., 51, 42–53, 2011.

Sharman, R. D., Trier, S. B., Lane, T. P., and Doyle, J. D.: Sources and dynamics of turbulence in the upper troposphere and lower stratosphere: A review, Geophys. Res. Lett., 39, L12803, doi:10.1029/2012GL051996, 2012.

Schneider, A., Gerding, M., and Lübken, F.-J.: Comparing turbulent parameters obtained from LITOS and radiosonde measurements, Atmos. Chem. Phys., 15, 2159–2166, doi:10.5194/acp-15-2159-2015, 2015.

Schumann, U., Konopka, P., Baumann, R., Busen, R., Gerz, T., Schlager, H., Schulte, P., and Volkert, H.: Estimate of diffusion parameters of aircraft exhaust plumes near the tropopause from nitric oxide and turbulence measurements, J. Geophys. Res., 100, 14147–14162, 1995.

Sheth, R., Kudeki, E., Lehmacher, G., Sarango, M., Woodman, R., Chau, J., Guo, L., and Reyes, P.: A high-resolution study of mesospheric fine structure with the Jicamarca MST radar, Ann. Geophys., 24, 1281–1293, doi:10.5194/angeo-24-1281-2006, 2006.

Stober, G., Latteck, R., Rapp, M., Singer, W., and Zecha, M.: MAARSY – the new MST radar on Andøya: First results of spaced antenna and Doppler measurements of atmospheric winds in the troposphere and mesosphere using a partial array, Adv. Radio Sci., 10, 291–298, doi:10.5194/ars-10-291-2012, 2012.

Stober, G., Sommer, S., Rapp, M., and Latteck, R.: Investigation of gravity waves using horizontally resolved radial velocity measurements, Atmos. Meas. Tech., 6, 2893–2905, doi:10.5194/amt-6-2893-2013, 2013.

Strelnikov, B., Lübken, F.-J., Rapp, M., Stober, G., Szewczyk, A., Strelnikova, I., Chau, J. L., Sommer, S., and Latteck, R.: Turbulence measurements in the mesosphere during the WADIS-1 sounding rocket campaign: Insight into horizontal variability, 40th COSPAR Scientific Assembly, 2–10 August 2014, Moscow, Russia, 2014.

Strelnikova, I., M. Rapp, Majority of PMSE spectral widths at UHF and VHF are compatible with a single scattering machanism, J. Atmos. Sol.-Terr. Phy., 73, 2142–2152, 2011.

Tatarskii, V. I.: Wave propagation in a turbulent medium, McGraw-Hill, New York, 1961.

Tatarskii, V. I.: The effects of the turbulent atmosphere on wave propagation, Israel Program for Scientific Translations, Jerusalem, 1971.

Thorpe, S. A.: Turbulence and mixing in a Scottish Lock, Philos. T. Roy. Soc. Lond. A, 286, 125–181, 1977.

Thorpe, S. A.: The turbulent ocean, Section 6.3.2, Cambridge University Press, Cambridge, UK, 2005.

VanZandt, T. E., Green, J. L., Gage, K. S., and Clark, W. L.: Vertical profiles of refractivity turbulence structure constant: Comparison of observations by the Sunset radar with a new theoretical model, Radio Sci., 13, 819–829, 1978.

Wyngaard, M.: Atmosphseric turbulence, Annu. Rev. Fluid Mech., 24, 205–234, 1992.

Wesson, J. C. and Gregg, M. C.: Mixing at Camarinal Sill in the Strait of Gibraltar, J. Geophys. Res., 99, 9847–9878, doi:10.1029/94JC00256, 1994.

Wilson, R., Luce, H., Dalaudier, F., and Lefrere, J.: Turbulence patch identification in potential density or temperature profiles, J. Atmos. Ocean Tech., 27, 977–993, doi:10.1175/2010JTECHA1357.1, 2010.

Wilson, R., Dalaudier, F., and Luce, H.: Can one detect small-scale turbulence from standard meteorological radiosondes?, Atmos. Meas. Tech., 4, 795–804, doi:10.5194/amt-4-795-2011, 2011.

Wilson, R., Luce, H., Hashiguchi, H., Shiotani, M., and Dalaudier, F.: On the effect of moisture on the detection of tropospheric turbulence from in situ measurements, Atmos. Meas. Tech., 6, 697–702, doi:10.5194/amt-6-697-2013, 2013.

Wilson, R., Luce, H., Hashiguchi, H., Nishi, N., and Yabuki, Y.: Energetics of persistent turbulent layers underneath mid-level clouds estimated from concurrent radar and radiosonde data, J. Atmos. Sol.-Terr. Phy., 118, 78–89, doi:10.1016/j.jastp.2014.01.005, 2014.

Woodman, R. F. and Guillen, A.: Radar observations of winds and turbulence in the stratosphere and mesosphere, J. Atmos. Sci., 31, 493–505, 1974.

Yagi, M. and Yasuda, I.: A modified method for estimating vertical profiles of turbulent dissipation rate using density inversions in the Kuril straits, J. Oceangr., 69, 203–214, 2013.

Yasuda, N.: Turbulent diffusivity and diurnal variations in the atmospheric boundary layer, Bound.-Lay. Meteorol., 43, 209–222, 1988.

Zink, F., Vincent, R. A., Murphy, E., and Cote, O.: Comparison of radar and in situ measurements of atmospheric turbulence, J. Geophys. Res., 109, D11108, doi:10.1029/2003JD003991, 2004.

Zovko-Rajak, D. and Lane, T. P.: The generation of near-cloud turbulence in idealized simulations, J. Atmos. Sci., 71, 2430–2451, 2014.